

Soft Soil Tire Model Development and Experimental Testing

*Dr. Corina Sandu¹, Mr. Eduardo Pinto², Mr. Scott Naranjo³, Dr. Paramsothy Jayakumar⁴,
Dr. Brant Ross⁵*

¹Virginia Tech, ²Virginia Tech, ³Virginia Tech, ⁴TARDEC, ⁵MotionPort
csandu@vt.edu

Abstract

Accurate and efficient tire models for soft soil operations are needed for mobility simulations of wheeled vehicles operating in off-road conditions. The tire model is essential in a vehicle model; the accuracy of the predicted tire forces and moments has a large impact on assessing the vehicle performance, reducing the number of stuck vehicles, avoiding rollovers, and developing advanced control strategies. While finite element method leads to the most detailed tire-soil interaction models, their complexity and extensive computational effort make them less than ideal for the applications envisioned, requiring hundreds of thousands of evaluations. Semi-analytical models such as the F-tire were developed for on-road applications. The semi-analytical soft-soil tire model developed in this study employs a similar construction as F-tire and adds an advanced tire-soil contact model. The tire is discretized in a user-defined number of lumped masses structured in three layers (two for the sidewall, one for the tread and belt), connected by elastic and damping elements connected in various configurations. Simulation results for several case studies performed with the tire model developed in this study are presented.

In this paper we also present the experimental work related to soil testing and tire instrumentation and testing, as needed to collect input data and to validate the new off-road tire model. The soil of interest is silty sand. Soil characterization, performed in collaboration with Schnabel Engineering, will be presented. A physical tire has been instrumented with sensors able to collect deflection information in real time. Such information, in addition to the information received from a string potentiometer, is critical in allowing the estimation of the true sinkage (versus just measuring the tire rut). Experimental results obtained for tire deflection with the instrumented tire on a quarter-car test rig will also be presented. Furthermore, since ensuring controlled, repeatable testing conditions is a very important aspect for data collection, the efforts made to guarantee that the normal load applied to the tire will stay constant during testing will also be discussed. The influence of tire and vehicle parameters and soil characteristics on the tire dynamics is also investigated.

Keywords: layout, typing instructions, references, nomenclature

1 Model Overview

The proposed soft soil tire model is intended for mobility, traction, and handling applications, and it can also be extended for durability studies. For such reasons, a complex semi-analytical tire modelling approach is the best fit.

The schematic of the proposed model can be observed in Fig. 1. It employs a discretized lumped mass approach that uses springs and dampers in multiple configurations to represent the different sections of the tire. One novelty of this model is that it is structured in three parallel planes, two of them representing the sidewalls (pictured in blue), and one of them represents the belt and tread (pictured in red) of the tire. By differentiating between the sidewall and the belt a more realistic applica-

Report Documentation Page

Form Approved
OMB No. 0704-0188

Public reporting burden for the collection of information is estimated to average 1 hour per response, including the time for reviewing instructions, searching existing data sources, gathering and maintaining the data needed, and completing and reviewing the collection of information. Send comments regarding this burden estimate or any other aspect of this collection of information, including suggestions for reducing this burden, to Washington Headquarters Services, Directorate for Information Operations and Reports, 1215 Jefferson Davis Highway, Suite 1204, Arlington VA 22202-4302. Respondents should be aware that notwithstanding any other provision of law, no person shall be subject to a penalty for failing to comply with a collection of information if it does not display a currently valid OMB control number.

1. REPORT DATE

14 JUL 2012

2. REPORT TYPE

Journal Article

3. DATES COVERED

14-10-2011 to 15-05-2012

4. TITLE AND SUBTITLE

Soft Soil Tire Model Development and Experimental Testing

5a. CONTRACT NUMBER

W56HZV-04-2-0001

5b. GRANT NUMBER

5c. PROGRAM ELEMENT NUMBER

6. AUTHOR(S)

Corina Sandu; Eduardo Pinto; Scott Naranjo; Paramsothy Jayakumar; Brant Ross

5d. PROJECT NUMBER

5e. TASK NUMBER

5f. WORK UNIT NUMBER

7. PERFORMING ORGANIZATION NAME(S) AND ADDRESS(ES)

Virginia Tech, 965 Prices Fork Road, Blacksburg, VA, 24061

8. PERFORMING ORGANIZATION REPORT NUMBER

; #23095

9. SPONSORING/MONITORING AGENCY NAME(S) AND ADDRESS(ES)

U.S. Army TARDEC, 6501 East Eleven Mile Rd, Warren, Mi, 48397-5000

10. SPONSOR/MONITOR'S ACRONYM(S)

TARDEC

11. SPONSOR/MONITOR'S REPORT NUMBER(S)

#23095

12. DISTRIBUTION/AVAILABILITY STATEMENT

Approved for public release; distribution unlimited

13. SUPPLEMENTARY NOTES

**For 12th European Regional Conference of the International Society for Terrain-Vehicle Systems ?
September 24-27, 2012, Pretoria, South Africa**

14. ABSTRACT

Accurate and efficient tire models for soft soil operations are needed for mobility simulations of wheeled vehicles operating in off-road conditions. The tire model is essential in a vehicle model; the accuracy of the predicted tire forces and moments has a large impact on assessing the vehicle performance, reducing the number of stuck vehicles, avoiding rollovers, and developing advanced control strategies. While finite element method leads to the most detailed tire-soil interaction models, their complexity and extensive computational effort make them less than ideal for the applications envisioned, requiring hundreds of thousands of evaluations. Semi-analytical models such as the F-tire were developed for on-road applications. The semi-analytical soft-soil tire model developed in this study employs a similar construction as F-tire and adds an advanced tire-soil contact model. The tire is discretized in a user-defined number of lumped masses structured in three layers (two for the sidewall, one for the tread and belt), connected by elastic and damping elements connected in various configurations. Simulation results for several case studies performed with the tire model developed in this study are presented.

15. SUBJECT TERMS

layout, typing instructions, references, nomenclature

16. SECURITY CLASSIFICATION OF:			17. LIMITATION OF ABSTRACT	18. NUMBER OF PAGES	19a. NAME OF RESPONSIBLE PERSON
a. REPORT unclassified	b. ABSTRACT unclassified	c. THIS PAGE unclassified	Public Release	33	

Standard Form 298 (Rev. 8-98)
Prescribed by ANSI Std Z39-18

tion of the local forces can be implemented, as can be seen in Fig. 1. Each plane consists of N_m number of masses; N_m is suggested between 80 and 100, but it is user-defined in an effort to increase the versatility of the model. This provides the user with flexibility in determining the resolution of the model.

The rigid wheel represents the rim of the tire and is directly connected to the sidewall layers. Thus, the wheel has six degrees of freedom; three translational and three rotational. On the other hand, each lumped mass has three degrees of motion: the translational motion in all directions. Moreover, there is relative motion between masses in the same plane and between masses in adjacent planes, as well. Relative motion is also allowed between lumped masses and the rigid wheel in the circumferential direction, which is another novelty introduced by this model. The total number of degrees of freedom of the model are,

$$DOF = 9N_m + 6 \quad (1)$$

Fig. 1: Diagram of the tire model. Note that all the soil forces are labeled in black.

The tire model requires several input parameters. The soil model also requires multiple input parameters. All the parameters needed for the tire and the soil model are listed in Section 3.1. The simulation inputs are: slip angle, slip ratio, camber angle, tire load, time for simulation, and finally either a driving torque or a longitudinal velocity. On the other hand, the outputs predicted by the model are: tire deformation, forces and moments in all directions, sinkage for sidewall and tread and belt layers and pressure distribution at the contact patch.

1.1 Sidewall Element

The sidewall element is more complex than the belt and tread element because it is directly connected to the rigid wheel. A diagram of the model can be observed in Fig. 2 and Fig. 3, and a description of each element can be found in Table 1. Notice how each sidewall mass has elastic and damping elements in all three directions. The mass of a single sidewall element ($m_{i,s}$) is calculated using Eq. (2).

$$m_{i,s} = \frac{0.5m_{sidewall}}{N_m} \quad (2)$$

The undeformed radius of each sidewall element is the undeformed radius of the tire minus the tread height as shown below,

$$R_s = R_u - h \quad (3)$$

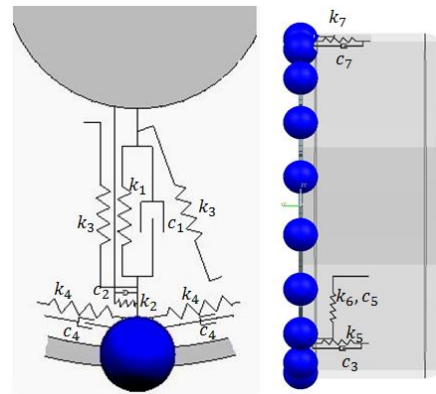


Fig. 2: Sidewall diagram. Left- the in-plane connections; right - the out-of-plane connections. (k_8 and c_6 not pictured)

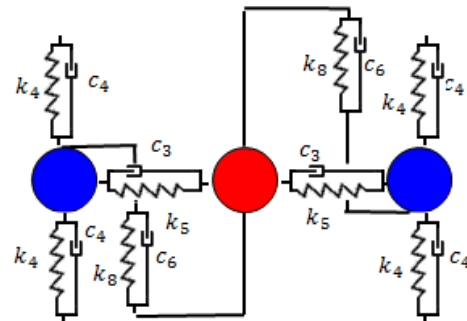


Fig. 3: Top view of the elements in the circumferential plane.

1.2 Belt and Tread Element

The belt and tread elements are different from the sidewall element. This is due to the

fact that the tread and belt layer is not directly connected to the rigid wheel. The diagram for the belt and tread element can be found in Fig. 4. It is important to note that there is an extra set of springs and dampers that connect the sidewall and belt and tread layers in the circumferential direction that is not shown in this figure. However, the extra set can be seen in Fig. 3. A description of each element can be found in Table 1.

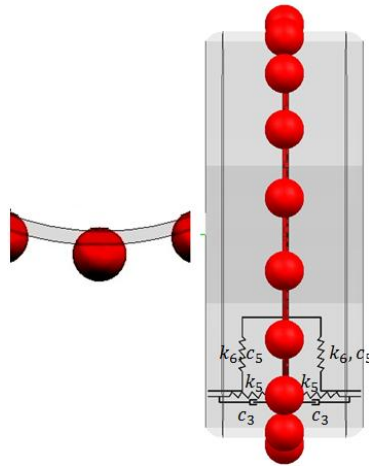


Fig. 4: Belt and tread element diagram. Left - in-plane view; right - out-of-plane view. (k_8 and c_8 not pictured)

It is also important to note that the undeformed radius of the belt and tread plane (R_u) is equal to what is traditionally understood by the undeformed radius of the tire (R_u); this is larger than the undeformed radius of the sidewall layer; thus the model accounts for the curved shape of the tire.

Table 1. Description of tire model elements

Element	Definition
k_1 & c_1	Sidewall radial spring stiffness and damping coefficient (in-plane)
k_2 & c_2	Wheel-sidewall circumferential spring stiffness and damping coefficient (in-plane)
k_3	Inter-element radial spring stiffness (in-plane)
k_4 & c_4	Circumferential inter-element spring stiffness and damping coefficient (in-plane)

k_5 & c_3	Lateral inter-element spring stiffness and damping coefficient (out-of-plane)
k_6 & c_5	Radial inter-element spring stiffness and damping coefficient (out-of-plane)
k_7 & c_7	Sidewall-wheel lateral spring stiffness and damping coefficient (out-of-plane)
k_8 & c_6	Circumferential inter-element spring stiffness and damping coefficient (out-of-plane)

The mass of a single belt and tread element ($m_{i,bt}$) is calculated using the equation,

$$m_{i,bt} = \frac{m_{tread} + m_{belt}}{N_m} \quad (4)$$

1.3 Coordinate systems

The model uses the following coordinate systems to describe the position of the wheel and of the lumped masses:

The X - Y - Z coordinate frame is the global reference frame. This global coordinate system follows the ISO 8855 standard, presented in Fig. 5. Therefore, the positive z -axis is pointing upwards.

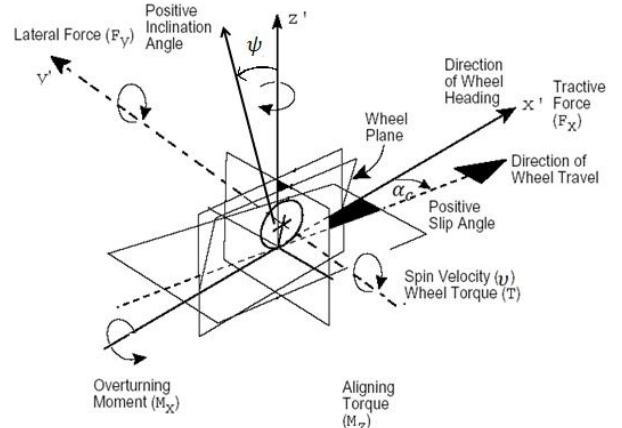


Fig. 5: ISO 8855 wheel coordinate system. Adapted from [1].

The x_0 - y_0 - z_0 is the local reference frame fixed to the rigid wheel.

Each lumped mass can be positioned with respect to the local wheel reference frame. Since the lumped masses have relative displacements in all three directions with respect to the rigid wheel, the springs and dampers included in the model along those directions will sustain deformations/displacement. To ease the calculation of deformation forces in the springs and damping forces in the dampers, these forces are computed along the directions of a local reference frame, x_i - y_i - z_i , attached to each of the lumped mass, as seen in Fig. 6. The lumped mass frames are oriented in such a way that the x_i reference frame points in the circumferential direction and the z_i reference points in the radial direction. Thus, it is worth noticing that these lumped mass reference frames are in fact always rotated with a fixed angle with respect to the directions of the position vectors that locate the mass in the rigid wheel reference frame.

The simulation is carried out in two steps, as explained below. To illustrate the use of the coordinate systems, two random masses were chosen in a two-dimensional space, the first one is denoted with a letter C and it is mass 1. The second is mass i and it is denoted by the letter A . Initially, the masses are located at positions A and C , which are identified by an angle θ_i , which is calculated using Eq. (5).

$$\theta_i = \frac{2\pi}{N_m}(i - 1) \quad (5)$$

The first step in the simulation is the rotation of the rigid wheel by an angle v . Thus, the masses move to locations A' and C' and have angles $\theta_i + v$. In the second step the lumped masses deform and go to locations A'' and C'' . Note that arbitrary deformations were chosen to illustrate the methodology used, in practice the masses can translate in all three directions. It is important to mention that the same method is used to locate the masses in each of the three planes.

Even though the lumped masses are allowed to translate in all directions, it is assumed that the displacements are very small,

such that a translation in a given direction doesn't affect those in other directions. This assumption can be made because we are using a very large number of masses. This is a valid assumption for this particular application because this model is to be run on relatively smooth surfaces at slow speeds, which guarantees that we will not be getting large deformations in the tire.

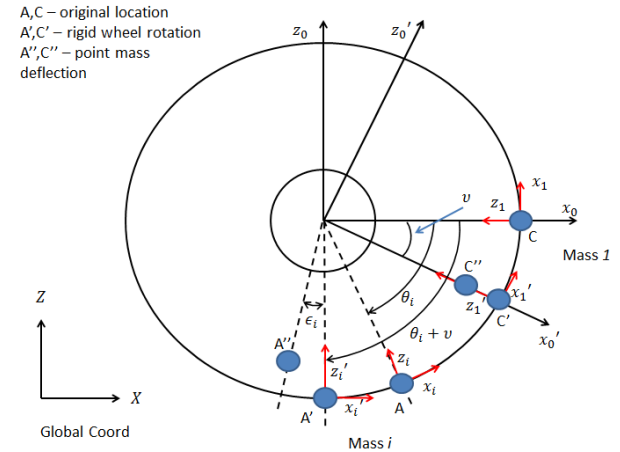


Fig. 6: Diagram of the coordinate systems used for one plane. Note that Y, y_0 and y_i are positive going outside of the page

1.4 Equations of motion

For illustrative purposes all equations presented in this section will be derived for N_m equal to 1. In the multibody dynamics community a vector of generalized coordinates \mathbf{q} represents the position and orientation of all bodies. The number of generalized coordinates for this model is $9N_m + 6$. Thus, for the condition that N_m is equal to 1, vector \mathbf{q} is defined by Eq. (6), where i is equal to 1. Note that if N_m is greater than 1 then the pattern will continue; left sidewall coordinates, right sidewall coordinates and finally belt and tread coordinates. It is important to mention that the first index (i) represents the mass number and the second one the layer (l- left sidewall, r- right sidewall, bt- belt and tread).

$$\mathbf{q} = [x_0 \ y_0 \ z_0 \ v \ \psi \ \alpha_c \ x_{i,l} \ y_{i,l} \ z_{i,l} \ x_{i,r} \ y_{i,r} \ z_{i,r} \ x_{i,bt} \ y_{i,bt} \ z_{i,bt}]^T \quad (6)$$

Having defined the generalized coordinate vector the equations of motion are defined by Eq. (7),

$$M\ddot{\mathbf{q}} + C\dot{\mathbf{q}} + K\mathbf{q} = \mathbf{F} \quad (7)$$

where the vector \mathbf{F} is defined by the applied external forces, C and K are the damping and stiffness matrices, and M is the generalized mass matrix,

$$M = \begin{bmatrix} M_0 & 0 & 0 & 0 \\ 0 & M_{i,l} & 0 & 0 \\ 0 & 0 & M_{i,r} & 0 \\ 0 & 0 & 0 & M_{i,bt} \end{bmatrix} \quad (8)$$

1.1.1 Equations of motion for the wheel

The mass matrix for the wheel is defined below,

$$M_0 = \begin{bmatrix} m_0 & 0 & 0 & 0 & 0 & 0 \\ 0 & m_0 & 0 & 0 & 0 & 0 \\ 0 & 0 & m_0 & 0 & 0 & 0 \\ 0 & 0 & 0 & I_y & 0 & 0 \\ 0 & 0 & 0 & 0 & I_x & 0 \\ 0 & 0 & 0 & 0 & 0 & I_z \end{bmatrix} \quad (9)$$

The moments of inertia (I_x , I_y and I_z) are calculated in Eq. (10) and (11) under the assumption that the wheel is a solid cylinder.

$$I_y = \frac{m_0 r_0^2}{2} \quad (10)$$

$$I_x = I_z = \frac{m_0(3r_0^2 + b^2)}{12} \quad (11)$$

In order to derive the equations of motion for the wheel it is important to first present the transformation matrices used to (i) change between reference frames and (ii) to orient the bodies in the three-dimensional space. The transformation matrix from the lumped mass reference frame to the global reference frame is described by Eq. (12), not that each lumped mass has a different transformation matrix.

$$A_1 = \begin{bmatrix} \sin(\theta_i + \nu) & 0 & -\cos(\theta_i + \nu) \\ 0 & 1 & 0 \\ \cos(\theta_i + \nu) & 0 & \sin(\theta_i + \nu) \end{bmatrix} \quad (12)$$

The rotation about the y-axis for each mass has the following transformation from the lumped mass reference frame to the global reference frame,

$$A_2 = \begin{bmatrix} \cos(\theta_i + \nu) & 0 & \sin(\theta_i + \nu) \\ 0 & 1 & 0 \\ -\sin(\theta_i + \nu) & 0 & \cos(\theta_i + \nu) \end{bmatrix} \quad (13)$$

The rotation about the x-axis from the lumped mass reference frame to the global reference frame is described by (14). It is pertinent to note that all masses have the same transformation.

$$A_3 = \begin{bmatrix} 1 & 0 & 0 \\ 0 & \cos(\psi) & \sin(\psi) \\ 0 & -\sin(\psi) & \cos(\psi) \end{bmatrix} \quad (14)$$

The rotation about the z-axis from the lumped mass reference frame to the global reference frame is also the same for all masses and it is described by equation (15).

$$A_4 = \begin{bmatrix} \cos(\alpha_c) & \sin(\alpha_c) & 0 \\ -\sin(\alpha_c) & \cos(\alpha_c) & 0 \\ 0 & 0 & 1 \end{bmatrix} \quad (15)$$

The forces acting on the wheel due to the springs and dampers are found in the Appendix A, Eq.(15)

The forces due to the springs and dampers acting on the wheel are the following in the global reference frame,

$$\begin{bmatrix} F_{x,0} \\ F_{y,0} \\ F_{z,0} \end{bmatrix} = \sum_{i=1}^{N_m} A_4 A_3 A_1 \begin{bmatrix} F_{2,i} \\ F_{7,i} \\ F_{1,i} \end{bmatrix} \quad (16)$$

Observing Eq. (16) it is evident that the forces in the springs and dampers connected to the wheel are multiplied by the transformation matrices to bring them back to the global reference frame. The order in which these matrices are multiplied is important. In this case, the tire is first rotated about the y-axis, this rotation is followed by a rotation of the x-axis and finally by a rotation of the z-axis. In the multibody dynamics community this would be described as an YXZ rotation.

The equations of motion for the wheel are shown in Eq. (17). The term W is the applied vertical load on the wheel center, while T is the applied driving torque, M_x is the applied torque about the x-axis, and M_z is the applied torque about the z-axis.

$$M_0 \ddot{q}_0 = \begin{bmatrix} F_{x,0} \\ F_{y,0} \\ F_{z,0} - m_0 g - W \\ T \\ M_x \\ M_z \end{bmatrix} \quad (17)$$

The following equations are used to obtain the forces and moments at the wheel in the global reference frame,

$$F_x = F_{x,0} \quad (18)$$

$$F_y = F_{y,0} \quad (19)$$

$$F_z = F_{z,0} \quad (20)$$

$$T_\phi = \sum_{i=1}^{N_m} F_{2,i} r_0 \quad (21)$$

$$T_\psi = \sum_{i=1}^{N_m} -F_{1,i} \sin(\theta_i + v) yy_i - F_{2,i} \cos(\theta_i + v) yy_i - F_{7,i} r_0 \text{sign}(\sin(\theta_i + v)) \quad (22)$$

$$T_{\alpha_c} = \sum_{i=1}^{N_m} -F_{1,i} \cos(\theta_i + v) yy_i + F_{2,i} \sin(\theta_i + v) yy_i - F_{7,i} r_0 \text{sign}(\cos(\theta_i + v)) \quad (23)$$

where yy_i is the relative location of the mass in the lateral direction with respect to the belt and tread layer. The command “*sign*” used in Eq. (22) and (23) returns a -1 if the corresponding element’s angle is less than zero, a 1 if it is greater than zero and a 0 if it equals zero.

1.1.2 Equations of motion - sidewalls

The mass matrix for the sidewalls is the same for both sidewalls since it is assumed that an equal number of masses is used in each sidewall.

$$M_{i,l} = M_{i,r} = \begin{bmatrix} m_{i,s} & 0 & 0 \\ 0 & m_{i,s} & 0 \\ 0 & 0 & m_{i,s} \end{bmatrix} \quad (24)$$

Thus, the forces acting on the springs and dampers connected to the left sidewall (Eq. (9-2), (9-3) and (9-4)) and right sidewall (Eq. (9-5), (9-6) and (9-7)) are presented in Appendix B.

The equations of motion for the left sidewall are defined by Eq. (25). The first terms are due to the internal forces in the springs and dampers attached to the mass, while the second set of terms represent the external force. The ground forces will be explained in detail in Section 2.

The equations of motion for the right sidewall are presented in Eq. (26)

$$M_{i,l} \ddot{q}_{i,l} = \begin{bmatrix} F_{x,i,l} + F_{4i,l} \\ F_{y,i,l} \\ F_{z,i,l} + F_{3,i,l} \end{bmatrix} + \begin{bmatrix} -m_{i,s} g \cos(\theta_i + v) + F_{xcp,i,l} \\ -F_{ycp,i,l} + F_{ybd,i,l} \\ -m_{i,s} g \sin(\theta_i + v) - m_i R_{i,l} \dot{v}^2 + \sigma_{n,i,l} \end{bmatrix} \quad (25)$$

$$M_{i,r} \ddot{q}_{i,r} = \begin{bmatrix} F_{x,i,r} + F_{4i,r} \\ F_{y,i,r} \\ F_{z,i,r} + F_{3,i,r} \end{bmatrix} + \begin{bmatrix} -m_{i,s} g \cos(\theta_i + v) + F_{xcp,i,r} \\ -F_{ycp,i,r} - F_{ybd,i,r} \\ -m_{i,s} g \sin(\theta_i + v) - m_i R_{i,r} \dot{v}^2 + \sigma_n \end{bmatrix} \quad (26)$$

Finally, the position vectors of the lumped masses in the left and right sidewall are described by Eq. (27) and (28).

$$\mathbf{r}_{i,l} = \begin{bmatrix} x_0 \\ y_0 \\ z_0 \end{bmatrix} + A_4 A_3 A_2 \begin{bmatrix} R_s \\ -\frac{W}{2} \\ 0 \end{bmatrix} \quad (27)$$

$$\mathbf{r}_{i,r} = \begin{bmatrix} x_0 \\ y_0 \\ z_0 \end{bmatrix} + A_4 A_3 A_2 \begin{bmatrix} R_s \\ \frac{W}{2} \\ 0 \end{bmatrix} + A_4 A_3 A_2 \begin{bmatrix} -z_{i,l} \\ y_{i,l} \\ x_{i,l} \end{bmatrix} + A_4 A_3 A_2 \begin{bmatrix} -z_{i,r} \\ y_{i,r} \\ x_{i,r} \end{bmatrix} \quad (28)$$

1.1.3 Equations of motion - belt and tread

The mass matrix for the belt and tread layer is defined below,

$$M_{i,bt} = \begin{bmatrix} m_{i,bt} & 0 & 0 \\ 0 & m_{i,bt} & 0 \\ 0 & 0 & m_{i,bt} \end{bmatrix} \quad (29)$$

The forces acting on the belt and tread elements due to the connected springs and dampers and equation of motion are described in Appendix C, Eq. (9-8) and (9-9), respectively.

Using the same formulation as the sidewall masses, the location of the lumped masses in the belt and tread layer is determined using the following Eq. (30)

$$\mathbf{r}_{i,bt} = \begin{bmatrix} x_0 \\ y_0 \\ z_0 \end{bmatrix} + A_4 A_3 A_2 \begin{bmatrix} R_u \\ 0 \\ 0 \end{bmatrix} + A_4 A_3 A_2 \begin{bmatrix} -z_{i,bt} \\ y_{i,bt} \\ x_{i,bt} \end{bmatrix} \quad (30)$$

2 Tire – soft soil interaction

This section reviews the soil model used; thus, it goes into the different formulations used to calculate the shear stresses and the normal pressure. Moreover, it goes into the details of how the interaction between the tire and the soil model is done. A general schematic of the different variables used is shown in Fig. 7.

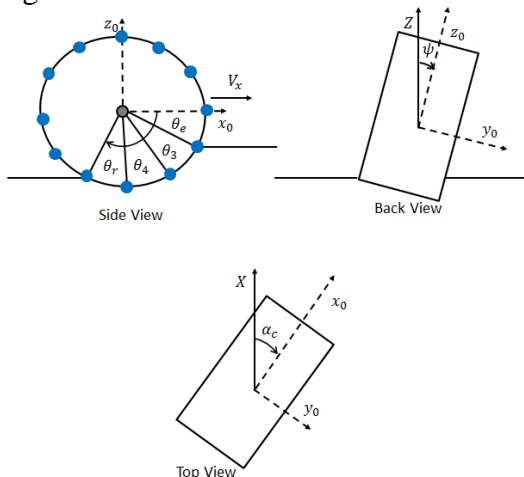


Fig. 7: Variables used to orient the tire

Most soils have elastic and plastic properties. Thus, the ideal behavior of an elasto-plastic material is described by Fig. 10. However, parameter identification for the

elastic properties of soils is difficult. As such, the theory of plasticity will be used to model the soil. This assumes that all deformation in the soil is permanent, so the rut and the sinkage are assumed to be the same.

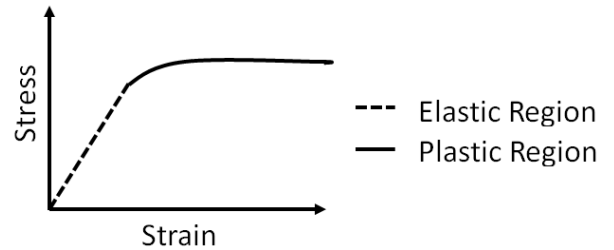


Fig. 8: Ideal behavior of an elasto-plastic material

By discretizing the tire into multiple masses and planes, a better resolution can be obtained for the forces in the contact patch. As shown in Fig. 9, the width of the tire (b) is divided into three sections that represent the sidewall and tread and belt layers. The formulation for the width of each section (w_i) is only dependent on the width of the tire,

$$w_i = \frac{b}{3} \quad (31)$$

On the other hand, the length (s_i) of each section is dependent on the deformed radius and the number of masses. The formulation gives Eq. (32).

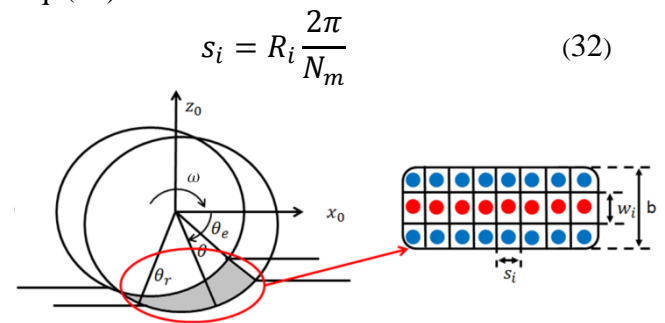


Fig. 9: Discretization of the contact patch

Before the formulation for the ground forces is presented it is pertinent to define the longitudinal slip or slip ratio (s_d). The slip is important when it comes to off-road locomotion because without any slip, motion would not be possible. The slip ratio in this thesis is calculated using the SAE standard, which is defined by the equation below,

$$s_d = 1 - \frac{V_x}{R_i \omega} \quad (33)$$

where V_x is the longitudinal velocity of the vehicle and ω is the radial velocity of the wheel.

2.1 Normal Ground Stress

One of the most important aspects of the interaction of the tire with soft soil is the computation of the normal pressure. The normal pressure is assumed to be perpendicular to the surface of the tire contact patch and it is dependent on the sinkage of the tire; a diagram of this contact force is shown in Fig. 10. The pressure distribution in the longitudinal direction is depicted in the diagram on the left of Fig. 10. At the entry angle the pressure in the radial direction is equal to zero and it increases until the location of peak pressure, which according to Reece and Wong [2] will shift with skidding or slipping; the pressure will then decrease until it reaches zero at the exit angle. On the other hand, the pressure distribution in the lateral direction is symmetric left to right, as shown in the diagram to the right of Fig. 10. However, for steering manoeuvres or straight line driving with a camber angle, the distribution is no longer symmetric about the centre. The shape of the contact patch will change from a rectangle to a trapezoidal shape.

In this study we implement an approach developed by Grahn [3, 4] to calculate the normal pressure (p_i), which is a method derived from Bekker's formulation[5], but with additional features; it includes the effects of longitudinal slip, vehicle velocity, and vertical penetration velocity. Grahn found that penetration velocity has a large influence on the pressure-sinkage relationship[6], thus motivating the need to account for it in our model.

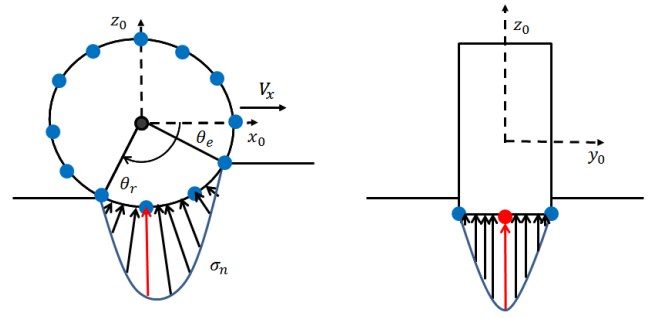


Fig. 10: Left- Longitudinal pressure distribution in the contact patch. Right – Lateral pressure distribution in the contact patch for straight line driving. The red arrow depicts the location of peak pressure

Using this methodology, the sinkage (z_i) is computed for each section i in the discretized tire model. The pressure in the radial direction on each mass can be computed using Eq. (35). Note that if $m = 0$ then these equations yield Bekker's quasi-static formulation [3]. Thus, the model uses Eq. (34) to calculate the pressure. Furthermore, it is important to note that Eq. (35) is only valid for penetration velocities larger than 0.1 cm/s. Thus, when this condition is not met the model uses (34).

$$p_i = \left(\frac{k_c}{s_i} + k_\phi \right) z_i^n \quad (34)$$

$$p_i = \left(\frac{k_c}{s_i} + k_\phi \right) z_i^n \left[\frac{V_x}{1 - s_d} \sin \left[\arccos \left(1 - \frac{z_0 - z_i}{R_i} \right) \right] \right]^m \quad (35)$$

Once the pressure is obtained at each section, the ground force ($\sigma_{n,i}$) is calculated using the equation shown in Eq. (36),

$$\sigma_{n,i} = p_i w_i s_i \quad (36)$$

As it was previously mentioned, the theory of plasticity is used to model the soil. Thus, the ground force is applied to the tire only when the vertical velocity of the wheel is either negative (tire sinks into the ground) or equal to zero (tire touches the surface).

The first step in the simulation is to load the tire. Solving the equations of motion yields the position, velocity and acceleration components of the wheel and lumped masses. Thus, the “find” command is used in

MATLAB to determine the first mass that has sinkage, which in turn returns the entry angle (θ_e). Similarly, the “*find*” command is also used to determine the last mass that has sinkage, yielding the exit angle (θ_r). Consequently, higher number of masses (N_m) will yield more accurate entry and exit angle.

The second step in the simulation is to start rolling the tire. This steps starts from the initial conditions identified in the dynamic settling performed in step one. For this scenario the entry angle is found in a similar manner. However, for the determination of the exit angle, the “*max*” command is used. This command will find the mass that has the highest sinkage, and thus, yield the exit angle. It is important to note that an algorithm is also used to determine if there are other masses that have the same maximum sinkage. This guarantees that if the contact patch is flat, the correct exit angle is found.

Having computed the normal pressure, the total drawbar pull (DP) of the tire is the following,

$$DP = \sum_{i=1}^{N_m} (F_{xcp,i,l} \sin \theta_{i,l} - \sigma_{n,i,l} \cos \theta_{i,l}) + \sum_{i=1}^{N_m} (F_{xcp,i,r} \sin \theta_{i,r} - \sigma_{n,i,r} \cos \theta_{i,r}) + \sum_{i=1}^{N_m} (F_{xcp,i,bt} \sin \theta_{i,bt} - \sigma_{n,i,bt} \cos \theta_{i,bt}) \quad (37)$$

where F_{xcp} is the lateral shear force, which is referred to as the shear trust in the terramechanics community. The computation of this force will be addressed in the following section. On the other hand, the ground force term is referred to as the compaction resistance.

In contrast, the computation of forces in the vertical direction is defined by Eq. (38),

$$W = \sum_{i=1}^{N_m} (F_{xcp,i,l} \cos \theta_{i,l} + \sigma_{n,i,l} \sin \theta_{i,l}) + \sum_{i=1}^{N_m} (F_{xcp,i,r} \cos \theta_{i,r} + \sigma_{n,i,r} \sin \theta_{i,r}) + \sum_{i=1}^{N_m} (F_{xcp,i,bt} \cos \theta_{i,bt} + \sigma_{n,i,bt} \sin \theta_{i,bt}) \quad (38)$$

where W is the normal load applied to the wheel.

2.2 Shear Stress

The shear stress allows the tire to have friction with the ground and be able to move. In this model the shear stress in the contact patch is computed using Janosi and Hanamoto’s approach [7]. This approach uses the tangential velocity or interface velocity to calculate the shear displacement in the longitudinal direction ($j_{x,i}$) for each mass in the contact patch. The soil shear displacement will be zero at the entry angle and it will increase until it reaches the exit angle.

$$j_{x,i} = R_i [(\theta_i - \theta_e) - (\cos \theta_e - \cos \theta_i) + s_d (\cos \theta_e - \cos \theta_i)] \quad (39)$$

On the other hand, the lateral shear displacement ($j_{y,i}$) is calculated using the lateral slip velocity. The lateral soil shear displacement behaves in the same way as in the longitudinal displacement where it starts at zero and keeps increasing until it reaches the exit angle.

$$j_{y,i} = R_i (1 - s_d) (\theta_i - \theta_e) \tan \alpha_c \quad (40)$$

Once the shear displacements are calculated, the longitudinal and lateral shear stress (τ_x and τ_y) can be evaluated using Eq. (41) and (42) respectively. This approach uses the Mohr-Coulomb soil strength failure criterion.

$$\tau_{x,i} = (c + \sigma_{n,i} \tan(\phi)) \left(1 - e^{-\frac{j_{x,i}}{k_x}}\right) \quad (41)$$

$$\tau_{y,i} = (c + \sigma_{n,i} \tan(\phi)) \left(1 - e^{-\frac{j_{y,i}}{k_y}}\right) \quad (42)$$

where c is the soil cohesion, ϕ is the internal angle of friction, and k_x and k_y are the longitudinal and lateral shear deformation modulus, respectively.

Equations (41) and (42) are valid for either pure longitudinal or pure lateral simulations. However, for combined slip scenarios the shear strength envelope of the soil needs to be considered. The approach followed in the thesis is consistent with that developed by Sandu and Chan in [8] where the Mohr-Coulomb soil strength failure criterion is used to define the maximum shear strength of the soil,

$$\tau_{max,i} = (c + \sigma_{n,i} \tan(\phi)) \quad (43)$$

Thus, the maximum shear stress envelope is characterized by an elliptical constraint defined by the following equation,

$$\left(\frac{\tau_{x,i}}{\tau_{max,i}}\right)^2 + \left(\frac{\tau_{y,i}}{\tau_{max,i}}\right)^2 \leq 1 \quad (44)$$

$$(\tau_{x,i})^2 + (\tau_{y,i})^2 = (\tau_{i,max})^2 \Big|_{\theta=\theta_a} \quad (45)$$

where θ_a is the angle where the stresses transition from sticking to sliding. Simplifying Eq. (45) yields Eq. (9-10), which can then be solved numerically to find θ_a , see Appendix D, Eq.(9-10). Consequently, the longitudinal and lateral shear stresses are defined by the following equations,

$$= \begin{cases} \tau_{max,i} \left(1 - e^{-\frac{j_{x,i}}{k_x}}\right) & \theta_e \geq \theta \geq \theta_a \\ \tau_{max,i} & \theta_a > \theta \geq \theta_r \end{cases} \quad (46)$$

$$= \begin{cases} \tau_{max,i} \left(1 - e^{-\frac{j_{y,i}}{k_y}}\right) & \theta_e \geq \theta \geq \theta_a \\ \tau_{max,i} & \theta_a > \theta \geq \theta_r \end{cases} \quad (47)$$

In principle, Eq. (46) and (47) guarantee that the shear strength of the soil never exceeds the failure envelope, however, the bulldozing force is not included in this formulation. Therefore, there might be times where the shear strength of the soil could be exceeded since

the bulldozing is added on top of the shear force. However, this simple approach is a good approximation, since the bulldozing stress is relatively small compared to the lateral shear stress.

Using the same approach as in the calculation of the normal force, the longitudinal and lateral shear forces acting on each mass are shown in Appendix D Eq. (9-11) and (9-12), which utilize μ_x and μ_y as the friction coefficients, computed using Eq. (48). The use of these coefficients is important because it limits the available traction at the contact patch to 1, thus, assuring that the shear forces will not exceed the shear envelope. Furthermore, since the shear forces are bounded, the solver doesn't encounter any convergence issues due to the sliding forces exceeding the maximum shear strength of the soil.

$$\mu_x = \mu_y = \min\left(\frac{\tau_{max,i}}{\sigma_{n,i}}, 1\right) \quad (48)$$

2.3 Bulldozing Force

The bulldozing effect is created when a volume of the soil in the contact patch is displaced to the sidewall of the tire when cornering. As such, a lateral force is created on the sidewall of the tire. A graphical representation of this phenomenon can be observed in Fig. 11.

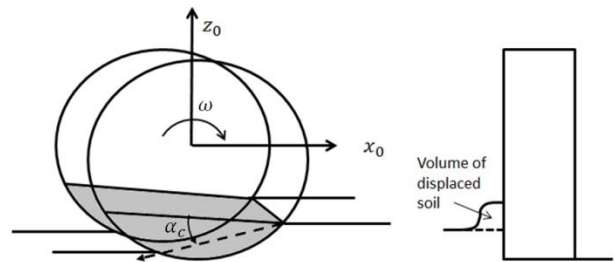


Fig. 11: Representation of the bulldozing force [8]

Few tire models account for the bulldozing component of the lateral force. Those that incorporate it applied it at the single mass that represents the contact patch. In the current study, due to the discretization of the tire, the bulldozing effect can be applied directly on the sidewall elements, thus increasing the realism of the model. However, it is important

to note that this bulldozing force can only be applied at the location of the discrete masses representing the sidewall.

Thus, a bulldozing force will be applied at each mass, which is also a more realistic representation. The formulation used to determine the bulldozing effect is based on the principle of passive ground resistance developed by Terzaghi, which is presented in [9-11]. This formulation has different dimensionless soil resistance coefficients (N_γ, N_c, N_q) that according to Wong [12] are dependent on the soil angle of friction ϕ . On the other hand, q is the surcharge load from the accumulated soil, which is calculated by assuming that the soil displaced in the lateral direction on each side of the wheel is the same as the volume of soil displaced by the area shaded in grey in Fig. 11. Thus, the surcharge load q is discretized by the method used in Fig. 12 and found using the equation below,

$$q_i = \frac{\gamma_s V_{soil,i}}{m_b z_i} \quad (49)$$

Where

$$m_b \approx \tan\left(\frac{\pi}{4} + \frac{\phi}{2}\right) \quad (50)$$

$$V_{soil,i} = A_i \lambda_i \tan(\alpha_c) \quad (51)$$

$$A_i = z_i s_i \quad (52)$$

$$\lambda_i = R_i (\cos \theta_e - \cos \theta_i) \quad (53)$$

The Terzaghi soil resistance coefficients [13] are found using the succeeding equations,

$$N_q = \frac{e^{2\left(\frac{3\pi}{4} - \frac{\phi}{2}\right) \tan \phi}}{2 \cos\left(\frac{\pi}{4} + \frac{\phi}{2}\right)^2} \quad (54)$$

$$N_c = \cot \phi (N_q - 1) \quad (55)$$

$$N_\gamma = 2(N_c + 1) \tan(\phi) \quad (56)$$

Once the surcharge is determined the bulldozing force is obtained using Eq. (57).

$$F_{ybd,i} = A_i (\gamma_s z_i^2 N_\gamma + c z_i N_c + q_i z_i N_q) \cos \psi \quad (57)$$

It is important to note that the bulldozing force is only applied to the outside sidewall when cornering, thus, assuming that no soil is displaced to the inside of the corner. Furthermore, it is also important to mention that it is estimated that Eq. (57) is applicable to slip angles under 45° .

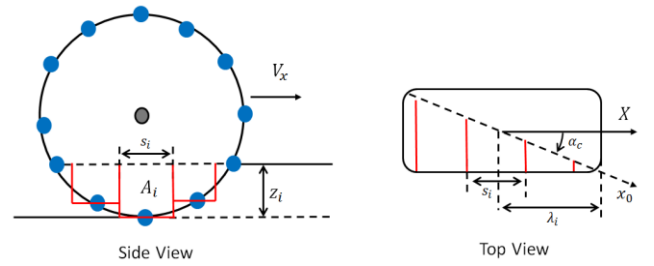


Fig. 12: Volume discretization for the calculation of the bulldozing force

The total lateral force generated by the tire is the summation of the lateral forces at each layer plus the lateral force created by a camber angle,

$$\begin{aligned} F_y &= F_{y,i,l} + F_{y,i,r} + F_{y,i,bt} + F_{camber} \\ &= \sum_{i=1}^{N_m} (-F_{ycp,i,l} + F_{ybd,i,l}) \\ &\quad + \sum_{i=1}^{N_m} (-F_{ycp,i,r} - F_{ybd,i,r}) \quad (58) \\ &\quad + \sum_{i=1}^{N_m} (-F_{ycp,i,l}) \\ &\quad + W \sin \psi \end{aligned}$$

2.4 Response to Repetitive Loading

The multi-pass is an important effect for soft soil interaction. The impact of a tire on the soil is dependent on a variety of factors. One such factor is the type of pass. A towed wheel will not alter the properties of the terrain in the same manner as a driven wheel, which induces larger changes [2]. The number of passes also has an influence on the terrain properties. Moreover, the slip ratio also affects the soil properties for repetitive loading scenarios.

Even though other researchers such as Harnisch et al. [14] have used Wong's approach with satisfactory results, this study will rely on the work of Holm [15] and Senatore [16] to predict the response to the multi-pass effect. The main idea of this approach is to estimate new parameters for the soil based on the pass type, slip, and number of passes.

Observing the results of Holm in [15] it is evident that the drawbar pull increases as the number of passes increases. This is mainly due to the fact that the compaction of each successive pass reduces the rolling resistance. Moreover, it is also evident that driven wheels will create more compaction than towed wheels, and thus, have higher drawbar pulls as the number of passes increases. Furthermore, it is also evident that the greatest variation in drawbar pull occurs between the first and second pass. Thus, the following relationships were developed to predict the change in soil conditions due to repetitive loading,

$$c = (c + c_{sd}) + c_1 s_d \quad (59)$$

$$\gamma_s = (\gamma_s + \gamma_{sd}) + \gamma_{s1} s_d \quad (60)$$

$$k_x = (k_x + k_{sd}) + k_{x1} s_d \quad (61)$$

where c_{sd} , γ_{sd} , and k_{sd} are parameters that are dependent on the type of pass, and c_1, γ_{s1} , and k_{x1} are functions of number of passes. In the case of a towed wheel, c_{sd} , γ_{sd} , and k_{sd} are equal to zero. On the other hand, for driven wheels their value is dependent on the wheel slip. Instead, for the parameters that are dependent on the number of passes, their value is equal to zero for the first pass and then it is contingent to the number of passes.

3 Case Studies and Simulation Results

This section first introduces the tire and soil parameters used for all the simulations. It then presents the results for the dynamic loading of the tire on rigid ground. The experimental results are compared to the simulation results in an effort to validate the tire deformation. The succeeding section presents a case study for dynamic settling on sandy loam. Consequently, case studies for pure lateral, pure longitudinal and combined slip scenarios are discussed. Finally, a case study for repetitive loading is analyzed.

3.1 Tire and Soil Parameters

The tire chosen for the validation of this model is Michelin LTX A/T 2 tire

(235/85R16), as shown in Fig. 13. According to Michelin of North America [17] this is an all season off-road tire for a light truck. It has a max load of 3042lbs (13,531N) at 80psi (551.6kPa) (load index 120) and a speed rating of R.



Fig. 13: Michelin LTX A/T 2 tire used for the model validation [17]

Due to the fact that we didn't have enough test data for this tire, the parameters used are a mixture of measured and approximated values. All damping coefficients were approximated based on a recommendation made by Mr. Michael Gipser from FTire; thus, the damping coefficients are between 1-3% of the stiffness values in the respective direction. The lateral tire stiffness was provided by Dr. Said Taheri as an approximation based on a very similar tire. The sidewall, belt and tread masses are estimations based on the total mass of the tire. The remaining values were obtained by experimental means, such as what is presented in Section 3.2.1.

Table 2: Tire parameters used for all simulations. Note that all these parameters need to be divided by the number of masses in contact and m_{total} is the total mass of the tire

Parameter	Value
m_{total}	19.83 kg
m_{rim}	11.52 kg
$m_{sidewall}$	$m_{total} * (2/3)$ kg
$m_{belt} + m_{tread}$	$m_{total} * (1/3)$ kg
b	0.2362 m
R_u	0.3937 m
h	0.0135 m
k_1	215,172 N/m
k_2	248,136 N/m
k_3	10^5 N/m
k_4	k_2 N/m
k_5	110,889 N/m
k_6	$5 * 10^5$ N/m
k_7	110,889 N/m

k_8	10^6 N/m
c_1	$k_1 * 0.03 \text{ Ns/m}$
c_2	$k_2 * 0.02 \text{ Ns/m}$
c_3	$k_3 * 0.01 \text{ Ns/m}$
c_4	$k_4 * 0.01 \text{ Ns/m}$
c_5	$k_5 * 0.05 \text{ Ns/m}$
c_6	$k_6 * 0.01 \text{ Ns/m}$
c_7	$k_7 * 0.01 \text{ Ns/m}$

The sandy loam parameters were found from a source written by Wong [12], since at the time this thesis was written the extraction of the soil parameters for the sandy loam used in the terramechanics rig was still on-going. It is important to note that the index of dynamic pressure could not be found either through experimental testing or literature; therefore, the Grahm pressure-sinkage equation, although implemented in the code, cannot be used. As such, all the simulations presented in this paper use the Bekker formulation. Grahm's equation can be employed as soon as the missing parameters are experimentally obtained.

Table 3: Soil Parameters used for all simulation

Parameter	Sandy Loam (11% Moisture Content)
Cohesion (c)	4830 Pa
Angle of friction (ϕ)	20°
Index of static pressure (n)	0.9
Coefficient of cohesion (k_c)	52,530 Pa
Coefficient of friction (k_ϕ)	1,127,970 Pa
Shear stress stiffness (k_x & k_y)	0.015 m
Index of dynamic pressure (m)	--
Soil Density (γ)	1258 kg/m ³

3.2 Dynamic Settling

The dynamic settling of the tire is an important step in the simulation because equilibrium needs to be attained between the tire and the soil. Moreover, the dynamic settling of the tire on a rigid surface was used to validate tire deformation.

3.2.1 Rigid Surface

The first step in the validation of the model was to compare the static deflection of the tire with the experimental data. The data used in this thesis was collected by Anake Umsrithong from Virginia Tech and it was collected for the same tire used in the soft soil validation. However, it is important to note that only the belt deformation will be validated since no data is available for the sidewall deformation. As such, for tire deflection validation purposes, the model was run using only the belt and tread plane.

The setup for these tests was simple. It consisted of loading and unloading the tire at different loads and then recording the deflection at 32 evenly spaced locations around the circumference of the tire. A picture of the test setup can be observed in Fig. 14.

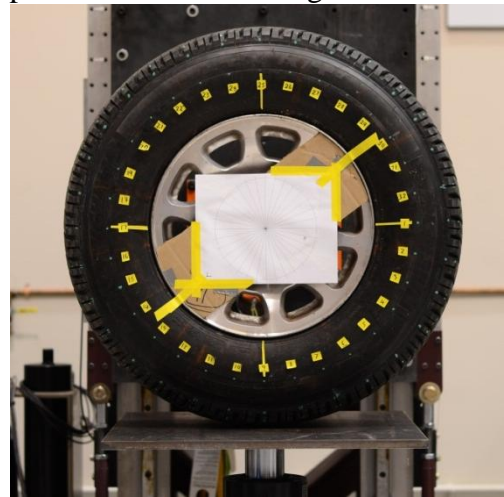


Fig. 14: Quarter car rig testing setup used to validate static deflection

During the loading of the tire, pictures were taken perpendicular to the tire surface such that image processing could be used to identify the deflections in the tire. Thus, two different loads were used to validate the model. The first one is an intermediate load of

5,128 N and the second is a high load of 11,022 N.

The comparison between the experimental and simulation results for the intermediate load can be observed in Fig. 15. Each circle represents the location of the masses in the simulation and the points marked in the tire. The deformation predicted by the simulation closely predicts the deformation observed in the experimental testing.

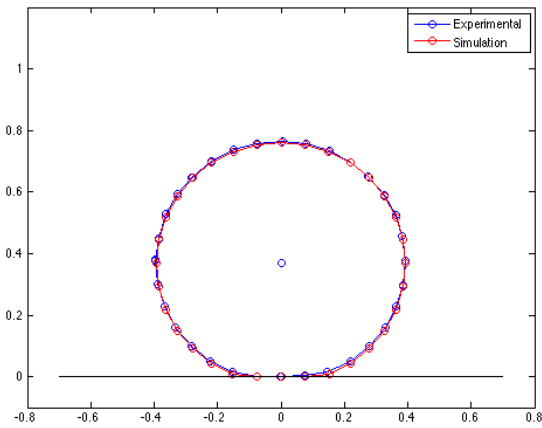


Fig. 15: Static deflection comparison for a rigid surface under an intermediate load (5128N)

Fig. 16 shows the deformation of the lumped masses in contact with the ground for both the radial and circumferential directions when a medium load (5,128 N) is applied. By analyzing the data it is evident that there is only a small deformation in the circumferential direction, while the largest radial deflection is around 2.5 cm.

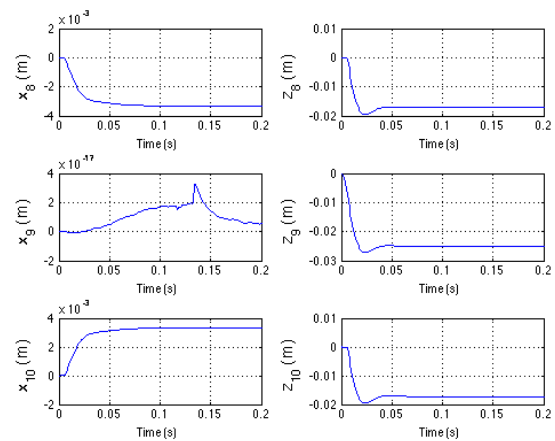


Fig. 16: Lumped mass deformations in the circumferential (x) and radial (z) direction for masses in contact (8,9,10) at a medium load (5128N)

The results for the high load also show good agreement with the experimental data as illustrated in Fig. 17. Moreover, by observing Fig. 17 and Fig. 18 it is evident that the deformation experienced by the tire is much larger for this higher load. Thus, the close resemblance between the collected data and the simulation suggests that the model is able to accurately predict tire deformation for static conditions.

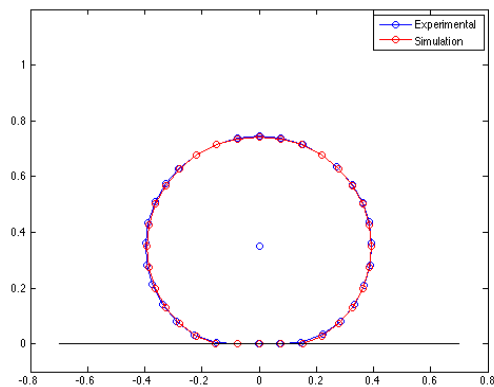


Fig. 17: Static deflection comparison for a rigid surface under high load (11,022 N)

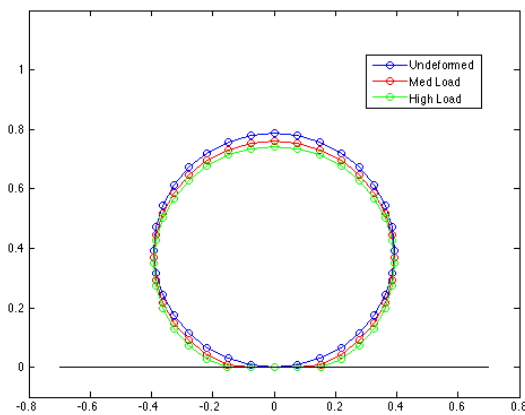


Fig. 18: Simulation comparison of tire deformation for different loads under a rigid surface

3.2.2 Soft Soil

This section will review the dynamic loading simulations that were done on sandy loam. The parameters for the sandy loam soil have already been presented in Table 3. Thus, the results presented in this section and the succeeding sections are more qualitative in nature. When available, the simulation will be compared to data collected for the same tire in the AVDL Terramechanics rig, which will be thoroughly explained in Section 4.1. Even though the sandy loam used in the simulation most closely matches the silky sand in the terramechanics rig, the soils are not identical. Therefore these comparisons should not be taken as a direct validation, but more of an indication that the tire model is properly predicting tire behavior for this type of soil. Moreover, as mentioned previously, due to lack of soil parameters, the pressure-sinkage

equation formulated by Grahn couldn't be used, as such, all the simulations in this investigation use Bekker's pressure-sinkage equation.

The dynamic loading of the tire is important because it is key to the analysis while equilibrium is reached between the tire and the ground. Thus, it is always the first step of the simulation. Fig. 19 shows a plot of the vertical displacement and velocity of the wheel center as the tire is dropped into the soft ground. As expected, it can be observed that the wheel center has a larger vertical displacement as the normal load is increased. Similarly, the vertical velocity follows the same behavior.

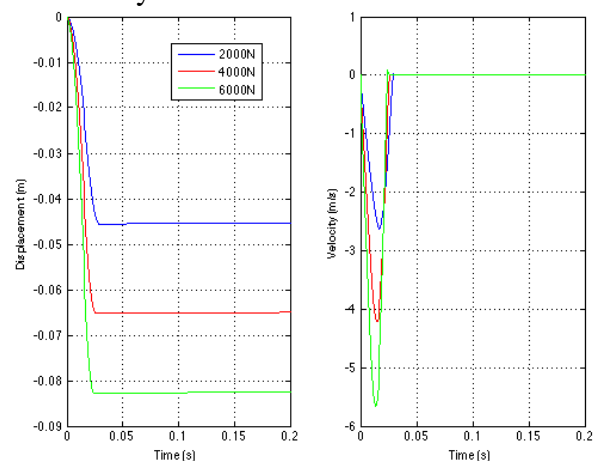


Fig. 19: Left-Vertical displacement; Right- Vertical velocity for the rigid wheel for the dynamic settling scenario

Fig. 20 shows the normal load fluctuation on the wheel center as the tire is dropped in the soft soil. As expected, the tire bounces slightly until it reaches equilibrium. However, by careful inspection it is evident that higher loads cause higher fluctuations. Moreover, due to the increased vertical velocity it is also observed that at higher loads the soil experiences higher pressure. It is important to note that different fluctuations were observed for different damping coefficients, however, since this thesis is not interested in the transient behavior of the tire this is not of great consequence.

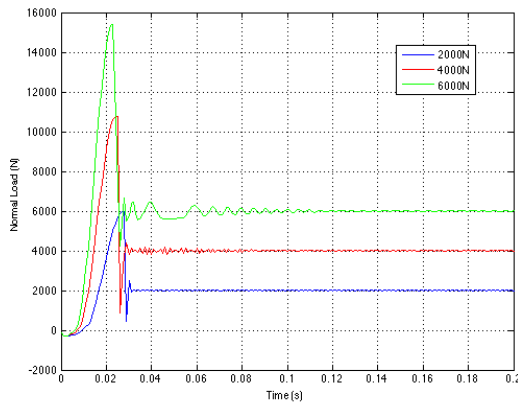


Fig. 20: Forces at the wheel centre for the dynamic loading scenario

Besides the displacements and forces at the wheel center the model is able to predict rut height for both the sidewall and tread and belt layers. It is important to note that since a plastic model was adopted for the soil, the rut height will be equal to the sinkage of the tire. Observing the sinkage of both the sidewalls and tread and belt layers in Fig. 21 it is evident that the belt and tread layer has a larger sinkage due to its larger radius. In Fig. 21 the simulation results were compared to experimental data gathered in the terramechanics rig using the silky sand discussed earlier.

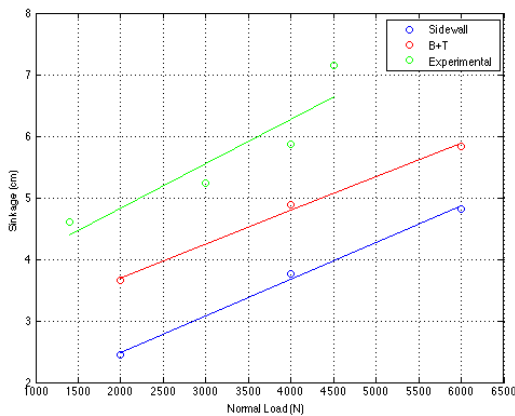


Fig. 21: Sinkage as a function of normal load for the dynamic loading case. Note that the simulation results are obtained using a Sandy Loam (11% moisture content), while the experimental data is obtained using a Silky Sand (~2% moisture content)

Fig. 22 shows the pressure distribution in the tire for a normal load of 6,000 N. The tire is divided into three layers; the middle layer represents the tread and belt layer, and the left and right layers the sidewalls. Each rectangle represents a lumped mass, thus, it is assumed

that the pressure is the same in any location of that specific rectangle. Moreover, the color bar represents the normal pressure exerted on each lumped mass in Pascal's. By inspection, it is evident that the pressure distribution is symmetrical left-to-right, however, we can see that the pressure is higher for the tread and belt layer, which makes sense since it has a larger sinkage.

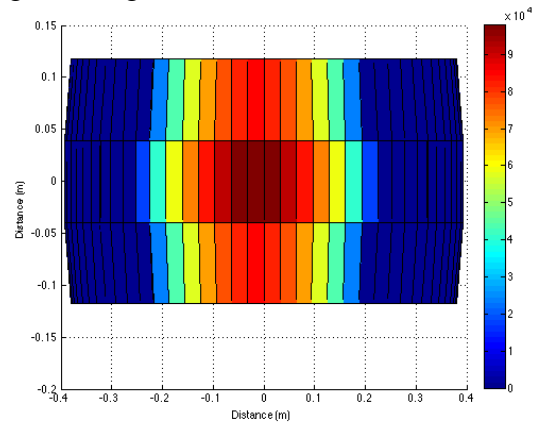


Fig. 22: Pressure distribution for the dynamic loading case using a normal load of 6,000 N, note that the color bar represents the normal pressure in Pascal's.

Finally, in Fig. 23 a diagram of the deformed tire is shown for the 6,000 N case. It can be observed that the tire experiences a considerable amount of deformation in the contact patch, which obviously increases with an increase in normal load.

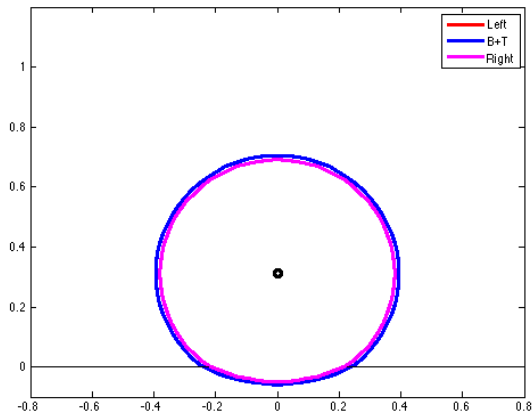


Fig. 23: Deformed tire for the dynamic loading case using a normal load of 6,000N

3.3 Steady State - Pure Longitudinal Slip

The pure longitudinal slip case study was run using the sandy loam. For all simulations, a longitudinal velocity of 2 m/s was inputted, thus, the results presented in this section show the steady-state behavior of the tire. Furthermore, 72 lumped masses per layer of the tire model were used for all simulations.

Tire sinkage is important when predicting the performance of off-road vehicles. Fig. 24 shows the simulation results for sidewall sinkage at a normal load of 2,000 N for different slips. At first inspection it is evident that there is a lot of variation in the data, however, this is due to the fact that masses lose and gain contact with the ground constantly. Obviously, if the number of masses is increased it is expected that these fluctuations will decrease.

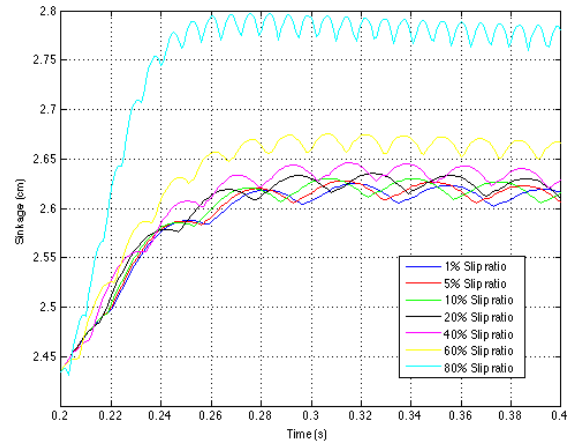


Fig. 24: Sidewall sinkage for different longitudinal slips at a normal load of 2,000 N and zero slip angle

In order to process the data, mean sinkage values were calculated for the different normal loads and slip ratios, which are presented in Fig. 25. In the same way as in the dynamic loading of the tire, the belt and tread layer has a higher sinkage due to its larger radius. It is also evident that sinkage has a slight increase for slip ratios of 1%-60%. However, for higher slip ratios higher sinkage is observed; this is referred as slip sinkage. Essentially, the slipping of the tire digs in the ground creating higher sinkage values.

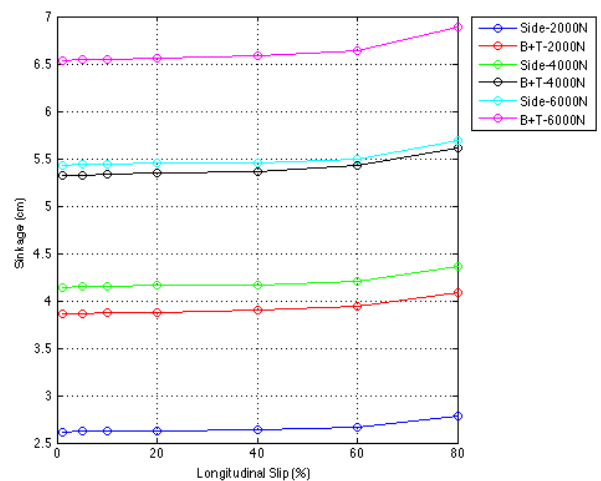


Fig. 25: Sinkage as a function of slip for different normal loads at zero slip angle

The drawbar pull is probably the most important measure when it comes to off-road locomotion; since it predicts vehicle mobility. Fig. 26 shows the drawbar pull as a function of time for different slip ratios at a normal load of 2,000 N. Similarly to Fig. 24, fluctua-

tions are observed in the data due to the loss and gain of contact of masses in the contact patch.

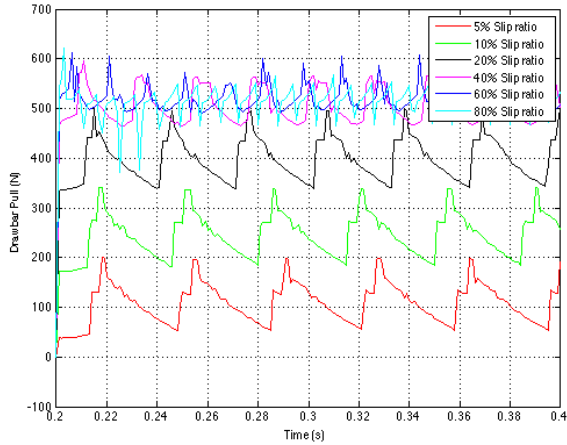


Fig. 26: Drawbar pull for different slip ratios at a normal load of 2,000 N

As it was previously mentioned, an increase in lumped masses will decrease fluctuations, and this can be observed in Fig. 27. This simulation was run using 200 masses, rather, than the standard 72 masses used for all other simulations. The fluctuations are significantly smaller for this simulation; however, the mean drawbar pull for the data set is quite close to the simulation with 72 masses.

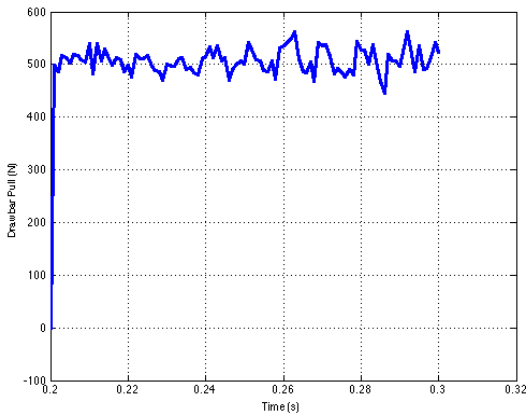


Fig. 27: Drawbar pull as a function of time for 200 masses, a normal load of 2,000 N, and a slip ratio of 30%.

In order to process the data presented in Fig. 26, mean averages were calculated for each normal load and slip ratio. The result is Fig. 28. As expected, an increase in normal load yields higher drawbar pulls. This is due to the fact that high loads create higher sinkage, thus, increasing the ground pressure and

the longitudinal shear stress. Moreover, it can be seen in Fig. 28 that the drawbar pull increases with longitudinal slip until it reaches 40%, where it starts to decrease. This transition point defines the location where rolling resistance stops being the limiting factor, and the wheel slip becomes the limiting factor. Thus, the location of this transition point is heavily based on soil properties.

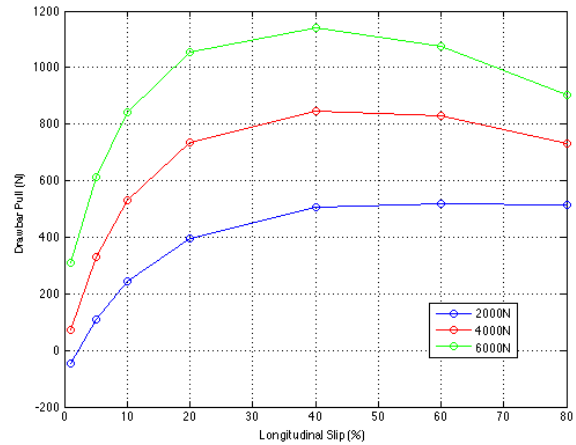


Fig. 28: Drawbar pull as a function of longitudinal slip for different normal loads

Comparing the simulation results of Fig. 28 with experimental data collected at AVDL in Fig. 29 for a rigid wheel on GRC1 lunar soil simulant it is evident that the data follows a similar trend.

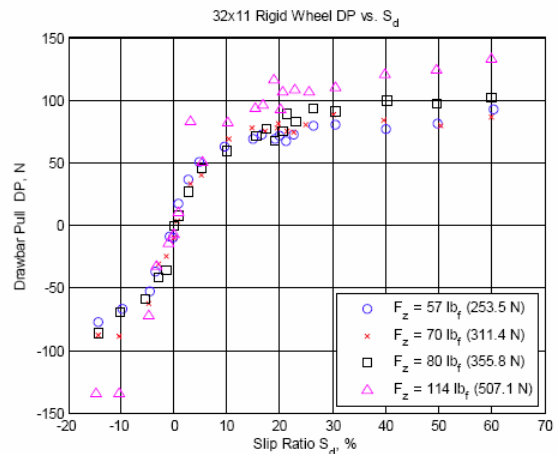


Fig. 29: Drawbar pull vs. slip ratio for experimental results on a rigid wheel collected at AVDL using GRC1 lunar soil simulant [18]

The driving torque is another important measure when it comes to off-road mobility. Knowing the required torque to

traverse a given terrain is important when determining the required power needed for a vehicle. Fig. 30 shows the driving torque required to traverse the terrain at various normal loads and slip ratios. As expected, higher normal load yields higher torque.

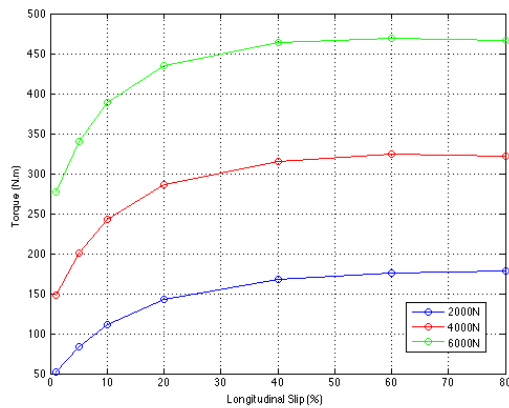


Fig. 30: Driving torque as a function of longitudinal slip for different normal loads

The camber angle has an important influence in the prediction of soft soil locomotion. Most importantly, the camber has a large influence on the pressure distribution in the contact patch. Fig. 31 shows the pressure distribution for a tire travelling at zero slip angle and zero camber. Similarly to Fig. 22, it can be observed that the normal pressure is symmetric left to right. On the other hand, Fig. 32 shows the pressure distribution for a tire travelling at 2° camber and zero slip angle. In this case, higher pressures are experienced by the right sidewall.

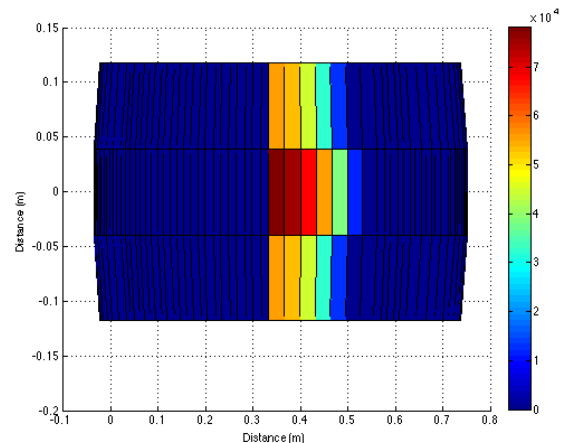


Fig. 31: Pressure distribution for a normal load of 2,000 N and a longitudinal slip of 10% at zero slip angle, the color bar represents the normal pressure in Pascal's

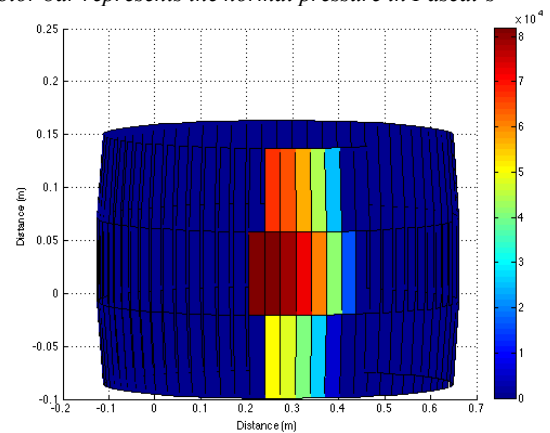


Fig. 32: Pressure distribution for a normal load of 2,000 N, a longitudinal slip of 10%, zero slip angle and a camber angle of 2° , the color bar represents the normal pressure in Pascal's

Furthermore, the camber angle creates additional lateral forces that contribute to the overturning moment. Fig. 33 shows both the driving torque and the overturning moment for a tire traveling with a camber angle. The driving torque is not affected by the camber angle; however, a small overturning moment can be observed. As it was previously mentioned, the fluctuations in the data are due to the change of masses in contact.

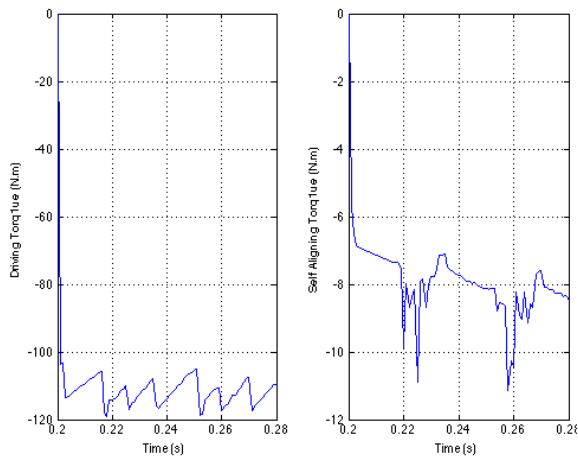


Fig. 33: Left- Driving torque and Right- overturning moment for a normal load of 2,000 N, a longitudinal slip of 10% and a camber angle of 2°

3.4 Steady State - Pure Lateral Slip

The next case that will be investigated is the pure lateral slip. Fig. 34 shows the lateral force as a function of slip angle for different normal loads. As expected, the lateral force increases with both slip angle and normal load. As it was shown in the previous section, higher normal load yields higher sinkage, thus, yielding higher lateral shear force. Likewise, the higher sinkage and slip angle will also increase the volume of soil displaced, consequently, increasing the bulldozing force. However, similarly to the drawbar pull plot in Fig. 28 there is a transition point where the forces reach the soils shear strength, thus, they level out.

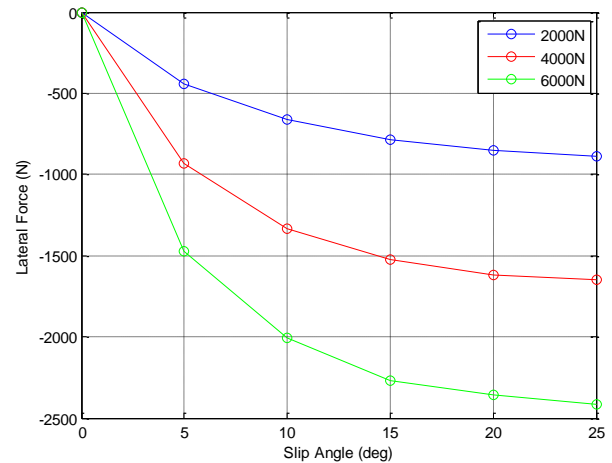


Fig. 34: Lateral force as a function of slip angle for different normal loads at zero longitudinal slip

Fig. 35 presents the overturning and self-aligning moments as a function of slip angle for different normal loads. It is evident that both moments follow similar patterns; both increase with slip angle and normal load. Contrary to the lateral force, the moments start leveling out at around 25° slip angle.

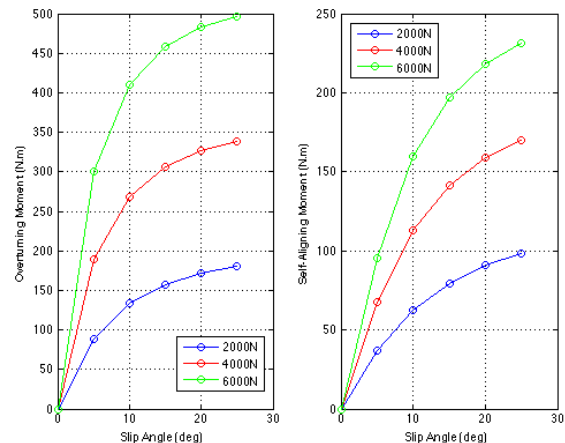


Fig. 35: Left- Overturning moment; Right- Self-aligning moment as a function of slip angle for different normal loads at zero longitudinal slip

Finally, Fig. 36 shows the pressure distribution for a steered tire. Due to the fact that camber is kept constant at 0°, the change in pressure from left to right is not that significant. However, some significant deformation due to the lateral shear and bulldozing forces is encountered in the lateral direction of the contact patch.

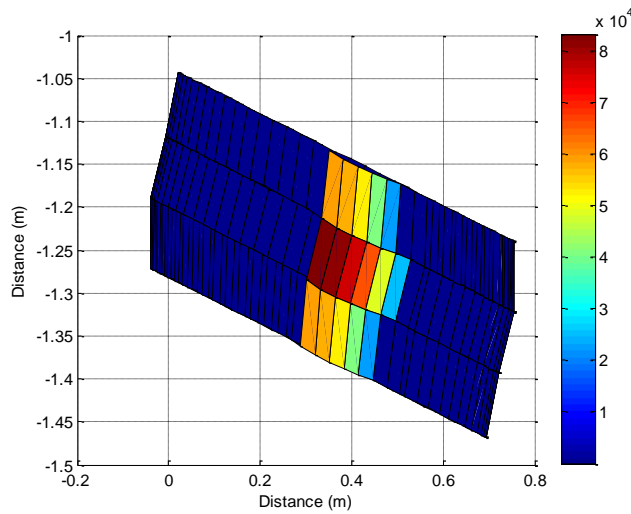


Fig. 36: Pressure distribution in the contact patch for a slip angle of 15°, a slip ratio of 0% and a normal load of 2,000 N. Note the deformation in the lateral direction of the contact patch

3.5 Combined Slip

Pure lateral and pure longitudinal case studies are quite common in tire modelling, however, vehicles are usually travel under combined slip scenario; therefore, it is important to account for combined slip in the model.

Fig. 37 shows the variation in drawbar pull for different slip angles at a normal load of 2,000 N. The figure shows that an increase in slip angle reduces the drawbar pull, which is consistent with the observations made by various researchers. This reduction is attributed to the fact that an increase in slip angle will increase the lateral shear stress, thus, reducing the longitudinal shear stress; since the combined forces cannot exceed the shear strength of the soil. However, it is important to note that at negative slip ratios the drawbar pull is higher than at their respective positive slips. This phenomena is attributed to the fact that braking will create higher sinkage, thus, increasing the longitudinal shear stress.

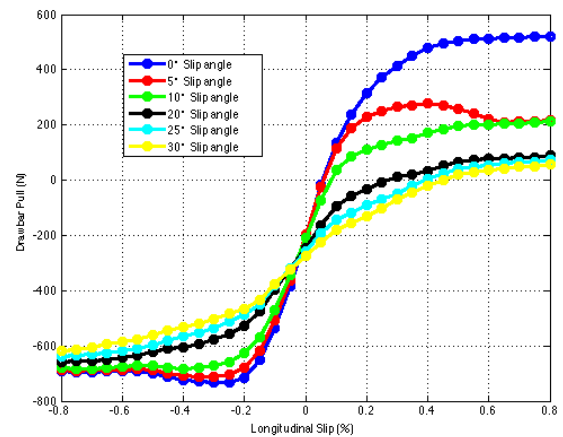


Fig. 37: Drawbar pull as a function of longitudinal slip for different slip angles at a normal load of 2,000 N

Fig. 38 shows the lateral force for different slip ratios at a normal load of 2,000 N. As anticipated, the lateral force decreases with an increase in slip ratio. Given the relationship between the longitudinal and the lateral shear stress, an increase in slip ratio will increase the longitudinal shear stress, thus reducing the lateral shear stress and vice versa.

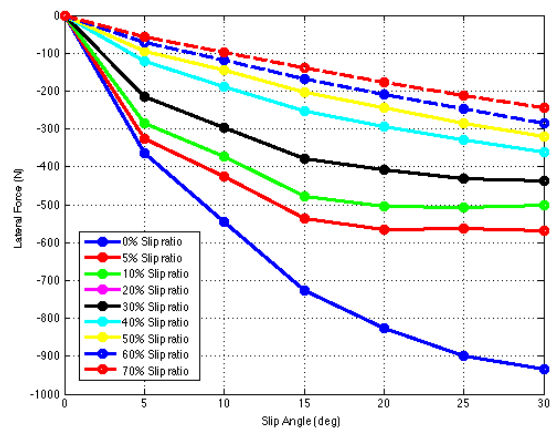


Fig. 38: Lateral force as a function of slip angle for different longitudinal slips at a normal load of 2,000 N

Fig. 39 shows the stress distribution at the contact patch for the combined slip scenario. As it can be observed, the longitudinal shear stress increases very quickly from the entry angle. However, at an angle θ_a , the tire starts to slide, which creates a drop in shear stress. Similarly, the lateral shear stress also increases until the angle θ_a , where it also drops. This decrease in shear stress at the angle θ_a guarantees that the Mohr-Coulomb failure criteria is upheld

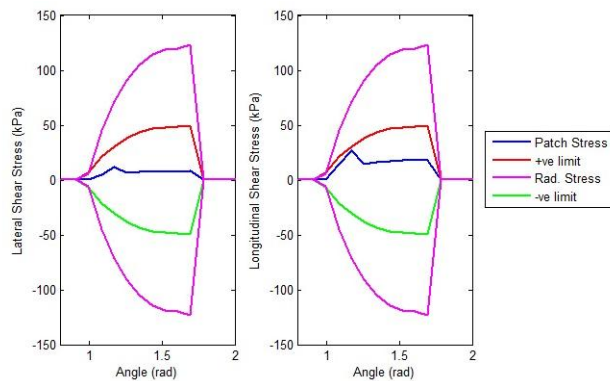


Fig. 39: Shear stress distribution for the belt and tread layer at a normal load of 4,000N, a slip angle of 10° and 40% slip ratio

3.6 Repetitive Loading

The following section will present the results for repetitive loading. Again, due to the unavailability of experimental data for repetitive loading, the results presented are more qualitative in nature. Fig. 40 shows the drawbar pull for a normal load of 2,000 N and a longitudinal slip of 20% for three consecutive driven tires. The simulation predicts that drawbar pull increases with each pass, which is due to the fact that less sinkage is experienced, thus, less rolling resistance. This also agrees with the experimental results collected by Holm in [15].

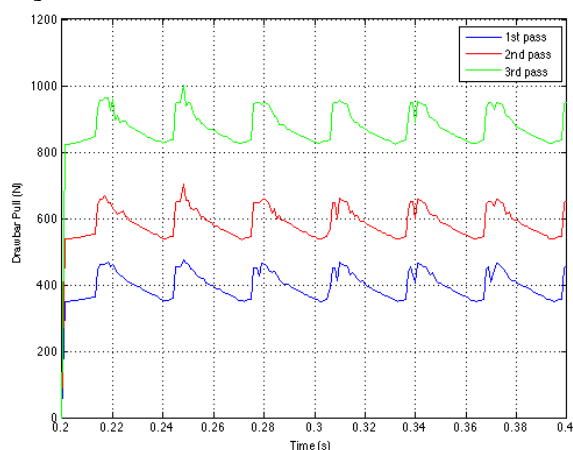


Fig. 40. Drawbar pull as a function of time for repetitive loading using a normal load of 2,000 N, zero slip angle and a longitudinal slip of 20%

4 Experimental Test Work

An exceptional amount of experimental validation work is required to ensure accurate and robust performance of the newly developed tire model. Therefore the following sections will highlight the indoor test rig where the main source of data collection is obtained, the tire test subject, additional instrumentation, test soil and laboratory soil parameter extraction.

4.1 Indoor Test Rig

The main test platform for investigating the tire-soil interaction for model validation is the Terramechanics Rig in the Advanced Vehicle Dynamics Lab at Virginia Tech. This single-wheeled test rig essentially simulates a rigidized-suspension, quarter-car model made to extensively investigate tire dynamics when applied to a wide variety of terrains, as shown in Fig. 41. The rig is driven by two motors – one provides the longitudinal velocity of the test wheel by actuating the belt system which moves the carriage (pictured in yellow in Fig. 41) along the test terrain, and the second motor controls the angular velocity of the test wheel; thus, allowing the user to predefine the different longitudinal slip test scenarios. The rig takes measurements via the Kistler P650 wheel hub sensor, which measures all three forces and moments attributed to the tire –soil interaction, wheel rotation, and angular velocity, also a string potentiometer is used to measure the wheel vertical travel. More information of the development and capabilities of the Terramechanics rig can be found in [19, 20].



Fig. 41: Terramechanics rig

4.2 Design of Experiments

A design of experiments (DOE) test matrix has been developed to efficiently accommodate the needs of the model validation and stay within the capabilities of the Terramechanics rig, as shown in Table 4. The DOE will be performed in a two stage, fraction factorial design to insure statistically relevant and repeatable results. The DOE was established with the following main interests in mind: high slip scenarios, similar parameters of an actual full-scale test vehicle, and practicality of soil conditioning. When developing the DOE, the military advisor of the project expressed the importance and interest to the military to test at large slip values. The actual test tire, the Michelin LT 235/85R-16 LTX A/T 2 E, as mentioned in Section 3.1, was chosen to correlate test results measured in the Terramechanics test rig and further validate the tire model with the results of an instrumented test vehicle at the University of Pretoria. For this reason, the normal load and inflation pressures were established to mimic that of the instrumented Land Rover Defender 110. The soil parameters were established to keep the soil preparation process, elaborated in section 3.2.9, repeatable and relevant, yet, less strenuous on the investigator.

Table 4: Design of experiments test matrix

Parameter	No. of Levels	Range
Slip Percentage	8	20 - 100%
Normal load	2	5000 N & 6000 N
Inflation Pressure	2	29 psi & 35 psi
Moisture Content	2	2-3% & ~9%
Compaction Resistance/ Cone Index	2	10.1 Kpa/mm & ~11.1 kPa/mm

Note, aside from the slip percentage, the other parameters have an arbitrary second level for further model validation.

4.3 Preliminary Test Results

Following the design of experiments, sets of data have been collected to reflect the lower level parameters of the test matrix, as shown in Fig. 42. These results are presented as normalized drawbar pull versus slip, for the low level parameters of the DOE. By inspection of Fig. 42, one can see that the drawbar pull follows the expected theoretical relationship with a change in slip.

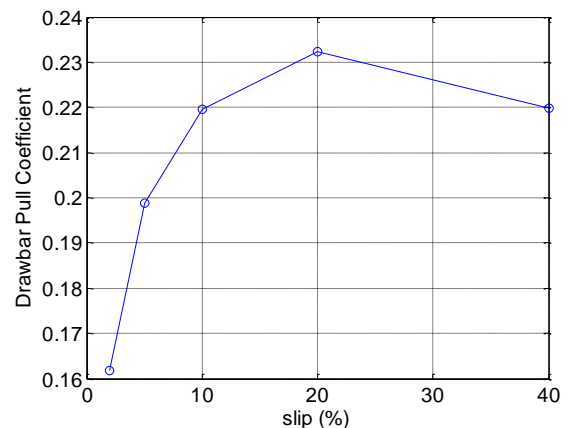


Fig. 42: Drawbar Pull Coefficient vs. slip at low DOE parameters

From this test work, it became evident that some equipment of the rig needed revision

and additional instrumentation, primarily the normal load and slip control. Throughout the testing, the normal load applied to the wheels varied too frequently to be able to directly validate the model performance with the collected data. Therefore in the following subsections, new instrumentation to control wheel normal and improve slip calculation will be discussed.

4.4 New Instrumentation

In order to accurately set and measure experimental parameters in the Terramechanics rig, it is vital to include more instrumentation. The new instrumentation and their purpose will be discussed in the following subsections.

3.2.3 Measure Deformed Rolling Radius

As mentioned in the previous section, the Terramechanics rig can run a predefined slip, assuming the user knows the rolling deformed radius. While this is normally determined through repetitive measures of the wheel's circumference after rolling at an assumed 0% slip condition, error is expected due to the nature of needing a deformed rolling radius to calculate slip. Therefore, a method to accurately measure the rolling deformed radius is taken upon the rig, which also gives an opportunity to measure the wheel contact patch deformation and max sinkage in soil.

The approach taken to measure the rolling deformed radius of a tire is to place multiple optical distance measuring sensors inside of a tire to measure the deflection of the tire inner liner. Multiple strategies and sensors have been used in the past to instrument tires to collect deformation data. Sensor technology used to instrument tires range among several, such as optical [21-25], ultrasonic sound [26], passive surface acoustic wave (SAW) [27], magnetic and piezoelectric[28-31].

The essential components that make the Wireless Internal Tire Sensors (WITS) possible are highlighted as the data collection, wireless data transmission, and power supply.

Starting with the data collection, multiple SHARP infrared emitting diodes (IREDs) are placed along different angular positions of the rim to collect as much tire deflection data as possible, as shown in Fig. 43. Given the small test path of the Terramechanics rig (roughly 4 meters), the test wheel commonly makes only two full rotations between testing so the more sensors, the more data. Also, due to the low speed testing conditions of the tire, normally 5-20 cm/s, tire imbalance is considered negligible; despite the assumption, efforts to balance the sensor placement is always taken into consideration.

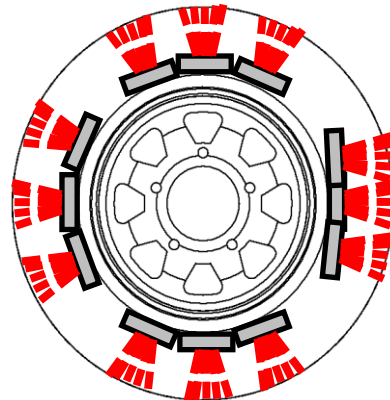


Fig. 43: Sample diagram of sensor arrangement inside a wheel

Each sensor is equipped with 5 IREDs covering a 25° range of deflection data, allowing a greater resolution of data collection. A control algorithm is required in order to obtain clean and stable data from the sensors[32], for this reason, an embedded microcontroller is placed inside the wheel with the sensors. The microcontroller, particularly the Arduino Mega 2560 R3, controls which sensors to use, collects data with a timestamp to be saved to an on-board memory card, and transmits the data wirelessly in intervals. Because of the control algorithm of the sensors and the 8-bit Analog to Digital Converter (ADC) of the Arduino Mega, the sample frequency is limited to, at most, 100 Hz. A triple axis accelerometer is also placed inside the wheel, primarily, to promote efficient data collection (by choosing to measure from sensors only at the contact patch) but can also be used to compute the test tire's camber and toe angles, respectively, as well as the angular velocity.

3.2.4 WITS – Wireless Capabilities

Due to the rotational nature of the wheel and sealed enclosure between the tire and rim, making the WITS system wireless reduces the complexity of the hardware configuration. This approach also lowers the overall cost of the system by avoiding the use of special pneumatically sealed feed through valves, wheel rim machining, and slip rings. Yet it in turn, raises the complexity of the software running the system and forces the system to be power efficient for long term running.

To fulfil the data transmission feature of the WITS system, the XBee Series 1 module, which utilizes the ZigBee/802.15.4 protocol, is chosen for its sufficiently-large broadcasting range (30 m) and relatively low power requirements (45 mA at 3.3 V)[33]. Another advantage is that interfacing an XBee module with the Arduino Mega is also relatively straightforward and heavily supported in the online mechatronics community.

The essential idea behind using the XBee module is to control what actions the Arduino Mega will follow such as collecting data for a test run, reading and extracting data from the memory card, and also changing parameters of the running Arduino Mega program.

3.2.5 WITS – Power

Again, because of the wireless nature and low-budget funding of the WITS system, a battery pack approach was taken to supply power to the WITS system. This method of power delivery was chosen for its ease of integration to the system and to avoid the clutter and cost of a slip rig, which would have forced the project to use a feed through pneumatically sealed valve.

The basic idea for the power delivery is to have a battery pack separately connected to the XBee module and will have a normally open connection to the Arduino Mega so that at the user's request, the XBee can be commanded to allow power flow to the Arduino Mega and sensors. Power conservation relays substantially on the XBee modules which will be in a "sleep" mode while the WITS system

is not in use; this mode of operation draws less than 50 μ A of current[33]. The XBee is configured to check for data transmission every hour, if it finds nothing, it will return to "sleep", if it receives data, it will turn the Arduino Mega on, via a relay, and send the received data to the Arduino Mega so that it can run the program requested by the user. The power switching duty of the XBee is accomplished by its simple digital input/out and analog input capabilities; another advantage of using the XBee module.

As for the batteries themselves, the WITS system will be powered by alkaline batteries. Alkaline batteries were chosen to keep the battery system simple and avoid the need of monitoring the charge/discharge cycle that common polymer lithium ion batteries require. To take make the WITS system more green, rechargeable AA batteries can be used instead of the current AA alkaline batteries. Lastly, to minimize weight offset caused by the battery packs, they will be evenly distributed around the wheel.

3.2.6 WITS – Sensor Validation

To ensure the accuracy of the tire deflection measured by the WITS system, a validation test was conducted at the Virginia Tech Performance Engineering Research Lab (PERL). The validation testing consisted of placing a wheel fitted with sensors on the PERL's Tire-coupled Quarter-Vehicle test rig and comparing the sensors measured tire deflection versus the deflection actuated by the test rig. This is the same test rig used in the early rig surface deflection test of Section 3.2.1.

Several tests were administered to see how well the sensors measured different tire deflections, such as a simple step input to a more dynamic sinusoidal wave fluctuation of the tire, as shown in Fig. 44.

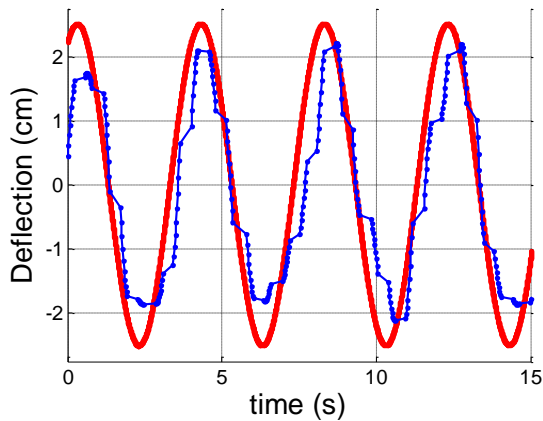


Fig. 44: 2.5cm 1/4 Hz Sinusoidal Input (RED) with WITS measurement (BLUE)

Fig. 44 illustrates that the WITS response is a fairly accurate measurement of the sinusoidal measurement of tire deflection. The amplitude difference of the WITS system can be attributed to the small tread deflection experienced as the rigid hydraulic actuation applies the load to the wheel. Also, the offset in time can be attributed to a slight difference in timestamps as both measurements were taken from different systems.

Note that the rig is also capable of measuring the vertical force applied to the wheel; however, this data was useless due to the air leak of the wheel. The air leak was due to early design efforts of the WITS system to feed the wires of the sensors through the rim.

Additional validation testing for the WITS system will be conducted on the rig itself using a Light Detection and Ranging (LIDAR) system. The fiber optic Doppler LIDAR system works by utilizing scattered light to collect data on a number of parameters, particularly for this test the relative velocity of the wheel angular and translational velocity. Knowing this calculation will allow an accurate measure of the slip, thus giving a clear measure of the deformed rolling radius.

3.2.7 Measure Max Sinkage

Measuring the instantaneous maximum sinkage of a rolling tire in soil is a great parameter of interest for model validation; despite the difficult nature of measuring this parameter, as opposed to the slightly different

rut depth. This project aims to measure max sinkage with new instrumentation. The max sinkage can be calculated with the use of the Terramechanics rig string potentiometer (measure vertical wheel displacement), the WITS system, and with the addition of an ultrasonic sound sensor to measure the soil height in the path of a rolling test tire. Fig. 45 illustrates how the max sinkage is calculated if the wheel displacement (h), the soil height ($h_{initial}$), and the deformed rolling radius ($R_{deformed}$) are known.

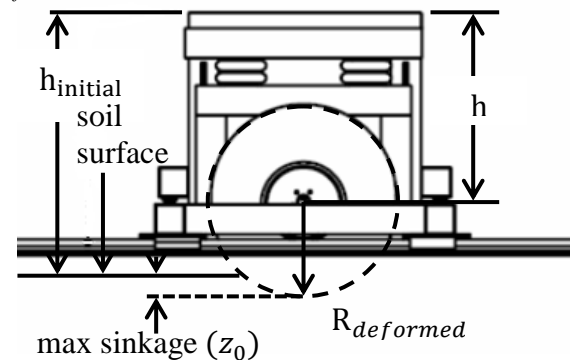


Fig. 45: Diagram for measuring max sinkage on Terramechanics Rig

Using said parameters allows the calculation of the max sinkage as shown in Eq. (62).

$$z_0 = (h + R_{deformed}) - h_{initial} \quad (62)$$

3.2.8 Normal Load Controller

As mentioned in Section 4.3 the variation in the applied wheel normal load while testing needs to be addressed. This is a result of passively applying a load to the test wheel via two triple-bellow air springs, shown in Fig. 41. Before each test run, air is applied until the desired normal load is achieved; however, as the wheel rolls over the test path, the wheel can sink or rise in the soil, thus changing the normal load. To counter the varying normal load, an active control system is being implemented to the system.

A proportional, integral, derivative (PID) control algorithm and an air proportional pneumatic control valve, Enfield Technologies' M1d, will be employed to keep active control of the wheel normal load. The basic idea of the setup is to command the M1d to either supply 10 bar of air to the air springs,

or exhaust the air; meanwhile, using the wheel hub sensor's vertical force readings as feedback to the controller. Given the valve's ability to supply air at a flow rate of approximately 2300 LPM (at 10 bar) in less than 5.6 ms response time to a change in signal input [34], the valve is expected to perform well enough to maintain a constant normal load on the wheel.

4.5 Soil Work

The novel aspect of the project is modeling the interaction of a tire over a deformable soil, specific to this study, silty sand; therefore, efforts to characterize the soil model with realistic parameters are of great importance. As demonstrated in the Section 2 and Table 3, multiple soil parameters are required to characterize the tire-soil interaction. Most of these parameters can be obtained with the bevameter technique [5], while others required additional experimental testing and a drive cylinder. Given the difficulty in obtaining a machine to follow the bevameter approach as well as performing the various amounts of additional experimental soil work, the AVDL has decided to subcontract Schnabel Engineering, a geotechnical engineering company, to extract soil properties of our sandy silt soil.

After consulting with one of Schnabel's associates, C.J. Smith, about the intended soil characterization of the project, the level of complexity and time required for accurate soil parameter extraction turned out to be much greater than expected. Also, the parameters of interest to the geotechnical world, (commonly civil engineers) varied greatly from the parameters needed from a terramechanics standpoint. For this reason the AVDL decided to launch an additional project to work alongside this modelling and validation project, on further soil parameter extraction and transformation to the soil model.

Nonetheless, lab soil testing has been conducted on the same soil and soil conditions that the Terramechanics rig will keep while performing tire-soil testing. To begin this

process, Schnabel had to measure the soil moisture and density that is expected for ideal testing conditions via their nuclear density gauge [35] in order to replicate the same scenario in the laboratory testing. The following subsection will explain the process of preparing the soil for ideal test conditions and the subsequent section will present some of the laboratory results of Schnabel.

3.2.9 Soil Preparation and Measurement

To ensure repeatable environmental test conditions, a four step soil preparation procedure was established. The main purpose of the soil preparation procedure is to remove any standing history of soil deformity, create a uniform level of soil, and compact the soil to a desired density. Multiple soil preparation procedures have been developed over the years, such as the automated "Mixing-and-Compaction" device in [36] and semi-automated procedure of [20]. Investigations of the impact the soil reconditioning procedure itself would have on the study results have been explored as well in [37, 38]. The procedure followed in the AVDL is similar to that of [20] but has been modified to cater to the different soil structure of silty sand. The process begins with tilling the soil using an electrical tilling machine; three passes along a 3 ft stretch are prepared to completely loosen the soil. The soil surface is then raked to provide a uniform and relatively smooth surface. Next the Terramechanics rig carriage is fitted with a smoothing blade and thoroughly flattens out the soil surface to a level, smooth surface. The final step requires making two passes with a variable-weight lawn roller to compact the soil.

Following the soil preparation procedure, the soil compaction and moisture is measured. A hand-held cone penetrometer is used to measure the compaction versus sinkage. The moisture content is measured using a simple ASTM standard [39] of microwaving the soil to measure the weight difference attributed to evaporated water. Averages of these measurements are taken to confirm overall con-

sistent soil parameters along the entire test path of prepared soil.

3.2.10 Soil Parameter Extraction

Under the advisory of C.J. Smith and Jody Priddy, a Ph. D student in the Geotechnical Engineering Program of the Civil & Environmental Engineering Dept. of VT, the test methods that would benefit the characterization of soil in the tire model were discussed and executed. To begin the laboratory testing, it was important to understand the physical makeup of the soil, which was initially believed to be “sandy loam” but turned out to be more of silty sand, according to the civil engineering and highway construction classification system [40, 41]. The following test performed was the standard proctor method which is used to understand the moisture-density relation of the soil [42]. This test revealed the maximum point of soil density versus moisture content. Similar to a cone penetrometer, a California Bearing Ratio (CBR) test was administered to measure the relative resistance to penetration of the soil [43]. The results of this data can be closely correlated with the cone penetration data obtained during testing in the Terramechanics rig. To investigate the shear strength of the soil, a triaxial compression test was implemented. The test was setup to measure the soil’s unconsolidated, undrained (UU) internal shear strength [44], again, to mimic the soil test conditions in tire-soil testing. The test was administered on three different specimens of varying confining stress (3 kPa, 10 kPa, and 21 kPa). Among the resulting data of triaxial testing of the three specimens the obtained soil stresses were plotted in Mohr circles in shear versus normal stress in the failure stress states; outlining a Mohr-Coulomb failure envelope defined by an internal friction angle of 17 degrees and cohesion of 9.7 kPa. Fig. 46 demonstrates the resulting Mohr circle plot.

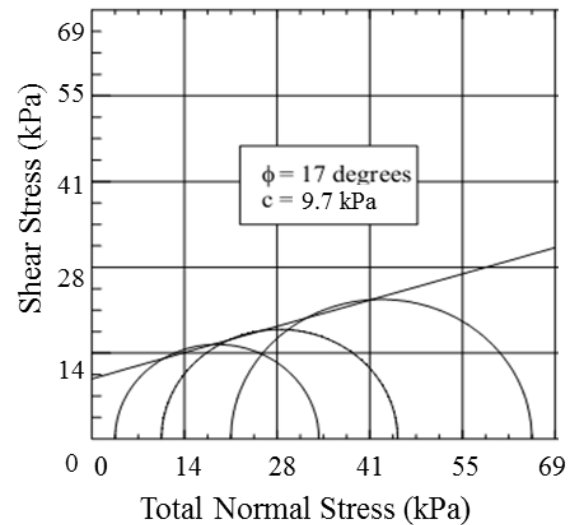


Fig. 46: Mohr Stress Circles at 2.5% Axial Strain Criterion; from Schnabel lab report

To measure the compressibility behaviour of the soil, a one-dimensional consolidation test was performed [45]. In this test, the soil was subjected to incremental, monotonic static from 12 kPa up to a maximum of 766 kPa, with unload-reload hysteresis cycles at 192 kPa and 766 kPa.

5 Conclusions

This paper presents a proposed semi-analytical soft soil tire model and its experimental validation methodology. The model is intended for traction, ride, handling, and durability applications. The work on the project is ongoing and simulation results as well as validation tests will be presented in future publications.

6 Acknowledgements

The work has been supported in part by the Automotive Research Center (ARC), a U.S. Army RDECOM Center of Excellence for Modeling and Simulation of Ground Vehicles led by the University of Michigan, and in part by NSF through award no. CMMI-0700278. The authors would also like to thank our ARC quad members for their continued support and guidance throughout the project.

7 Nomenclature

b	Tire width	s_d	Longitudinal slip
β	Initial radius approximation dimensionless variable	V_x	Vehicle longitudinal velocity
c	Soil cohesion	z_0	Maximum sinkage
c_0	Experimental constant used to determine θ_m	n	Pressure-sinkage index
c_i	Multipass experimental parameter	m	Penetration velocity exponent
c_{sd}	Multipass experimental parameter	m_{bead}	Bead mass
c_m	Experimental constant used to determine θ_m	$m_{i,bt}$	Belt plus tread element mass
δ	Tire deformation	m_{thread}	Tread mass
k_x	Longitudinal shear deformation modulus	m_{belt}	Belt mass
k_y	Lateral shear deformation modulus	$m_{sidewall}$	Total sidewall mass
k_{xi}	Multipass experimental parameter	$m_{i,s}$	Sidewall element mass
k_{sd}	Multipass experimental parameter	m_{wheel}	Wheel mass
k_0	Static modulus of soil deformation	N_m	Number of masses
k_1	Sidewall radial spring stiffness (in-plane)	σ_n	Normal stress
k_2	Wheel-sidewall radial spring stiffness (in-plane)	τ_x	Longitudinal shear stress
k_3	Inter-element radial spring stiffness (in-plane)	τ_y	Lateral shear stress
k_4	Tangential inter-element spring stiffness (in-plane)	j_x	Longitudinal shear displacement
k_5	Lateral inter-element spring stiffness (out-of-plane)	j_y	Lateral shear displacement
k_6	Radial inter-element spring stiffness (out-of-plane)	p	Radial pressure
c_1	Sidewall radial damping (in-plane)	p_t	Tire internal pressure
c_2	Sidewall circumferential damping (in-plane)	ϕ	Soil angle of internal friction
c_3	Lateral inter-element damping (out-of-plane)	γ	Soil density
c_4	Wheel-sidewall radial damping (in-plane)	γ_s	Unit weight of soil
R_l	Loaded radius	γ_{si}	Multipass experimental parameter
R_u	Un-deformed radius	γ_{sd}	Multipass experimental parameter
$R_{deformed}$	Deformed rolling radius	N_γ	Soil specific weight coefficient
		N_c	Soil cohesion coefficient
		N_q	Soil surcharge load coefficient
		q	Surcharge load from accumulated bulldozed soil
		z	Sinkage
		ζ	Initial radius approximation dimensionless variable

\dot{z}	Vertical penetration velocity	θ_m	Angle of maximum normal stress
z_0	Maximum sinkage	θ_r	Exit angle
δ_f	Angle of friction between soil and tire	α_c	Slip angle
θ	Central angle describing mass position	y	Lateral distance from tire center
θ_a	Angle of transition	ψ	Toe Angle
θ_b	Trailing Edge Angle		
θ_e	Entry angle		
θ_f	Leading edge angle		

8 References

- [1] AdamsMSC Users Manual Software. MSC Software; 2011.
- [2] **Wong JY, and Reece, A. R.** . 1967 *Prediction of Rigid Wheel Performance Based on the Analysis of Soil-Wheel Stresses. Part I. Performance of Driven Rigid Wheels*. Journal of Terramechanics.4:81-98.
- [3] **Grahn M.** 1991 *Prediction of Sinkage and Rolling Resistance for Off-The-Road Vehicles Considering Penetration Velocity*. Journal of Terramechanics.28:339-47.
- [4] **Grahn M.** Investigation of the Influence of Penetration Velocity on the Pressure/Sinkage Relationship. Proceedings of the 9th International ISTVS Conference. Barcelona, Spain1987.
- [5] **Wong JY.** Theory of ground vehicles. 4th ed. Hoboken, N.J.: Wiley; 2008.
- [6] **Fassbender FR, Fervers, C. W., and Harnisch, C.** 1997 *"Approaches to Predict the Vehicle Dynamics on Soft Soil"* Vehicle System Dynamics.27:173-88.
- [7]**Janosi Z, and Hanamoto, B.** Analytical determination of draw bar pull as a function of slip for tracked vehicles in deformable soils. 1st Int Conf of the International Society for Terrain-Vehicles Systems. Turin, Italy1961.
- [8] **Chan BJ.** 2008. *Development of an Off-Road Capable Tire Model for Vehicle Dynamic Simulations* [Ph. D Dissertation]. Blacksburg, VA: Virginia Polytechnic Institute and State University.
- [9] **Schwanghart H.** 1968 *Lateral Forces on Steered Tyres in Loose Soil*. Journal of Terramechanics.5:9-29.
- [10] **Hettiaratchi DRP, and Reece, A. R.** 1967 *Symmetrical Three-Dimensional Soil Failure*. Journal of Terramechanics.4:45-67.
- [11] **Hettiaratchi DRP, and Reece, A. R.** 1974 *The Calculation of Passive Soil Resistance*. Geotechnique.24:289-310.
- [12] Wong JY. Theory of Ground Vehicles. 4th ed ed. Hoboken, NJ: John Wiley & Sons; 2008.
- [13] Terzaghi K. Theoretical Soil Mechanics. 1st Edition ed: Wiley & Sons; 1943.
- [14] **Harnisch C, Lach, B., Jakobs, R., Troulis, M., and Nehls, O.** 2005 *A new tyre soil interaction model for vehicle simulation on deformable ground*. International Journal of Vehicle Mechanics and Mobility.43:384-94.
- [15] **Holm IC.** 1969 *Multi-Pass Behaviour of Pneumatic Tires*. Journal of Terramechanics.6:47-71.
- [16] **Senatore C.** 2010. *Prediction of mobility, handling, and tractive efficiency of wheeled off-road vehicles* [Ph. D Dissertation]. Blacksburg, VA: Virginia Polytechnic Institute and State University.
- [17] Organic Rose Care. Organic Rose Care; 2012.
- [18] **Taylor BP.** 2009. *Experimental Evaluation and Semi-Empirical Modeling of the Tractive Performance of Rigid and Flexible Wheels on Lunar Soil Simulant*. Blacksburg: Virginia Polytechnic Institute and State University.
- [19] **Biggans JS.** 2007. *Design of a Terramechanics Rig*. Blacksburg: Virginia Tech.
- [20] **Taylor B.** 2009. *Experimental Evaluation and Semi-Empirical Modeling of the Tractive Performance of Rigid and Flexible Wheels on Lunar Soil Simulant*. Blacksburg: Virginia Tech.
- [21] **Tuononen AJ.** 2008 *Optical position detection to measure tyre carcass deflections*. Veh Syst Dyn.46:471.
- [22] **Tuononen AJaH, L.** 2008 *Optical position detection sensor to measure tyre carcass deflections in aquaplaning*. Int J Veh Syst Modelling Test.3:189.
- [23] **Tuononen AJ.** 2009 *On-board estimation of dynamic tyre forces from optically measured tyre carcass deflections*. Heavy Veh Syst.16:362.
- [24] **Matsuzaki R, Hiraoka, N., Todoroki, A. and Mizutani, Y.** 2010 *Optical 3D deformation measurement utilizing non-planar surface for the development of an 'intelligent tire'*. J Solid Mech Mater Eng.4:520.
- [25] **Tuononen AJ.** 2011 *Laser triangulation to measure the carcass deflections of a rolling tire*. Measurement science & technology.22:125304-.
- [26] **Magori V. MVRaSN.** 1998 *On-line determination of tyre deformation, a novel sensor*

- principle. IEEE Ultrasonics Symp Proc.485-8.
- [27] **Pohl A, Steindl, R. and Reindl, L.** 1999 *The 'intelligent tire' utilizing passive saw sensors—measurement of tire friction*. IEEE Trans Instrum Meas.48:1041.
- [28] **Breuer B. EUaR.** 1992 *Measurement of tyre/road-friction ahead of the car and inside the tyre*. AVEC'92 (Yokohama).347.
- [29] **Becherer T.** 1998 *The Sidewall Torsion Sensor System*. 2. DarmstädterReifenkolloquium.130.
- [30] **Yilmazoglu O.** 2001 *Integrated InAs/GaSb 3D magnetic field sensors for 'the intelligent tire'*. Sensors Actuators.94:59.
- [31] **Singh K.** 2012. *Development of an Intelligent Tire Based Tire - Vehicle State Estimator for Application to Global Chassis Control* [Master]: Virginia Tech.
- [32] **SHARP.** 2006 *Wide angle Distance Measuring Sensor Unit*. GP2Y3A001K0F Datasheet.
- [33] **DIGI.** 2009 *XBee ZigBee/802.15.4 Modules*. Datasheet.
- [34] **Technologies E.** 2011 *M1d - Proportional Pneumatic Control Valve*. Datasheet.3.
- [35] **D6938.** *Standard Test Method for In-Place Density and Water Content of Soil and Soil-Aggregate by Nuclear Methods (Shallow Depth)*. Annual Book of ASTM Standards.4.09.
- [36] **Kawase Y, Nakashima, H., and Oida, A.** 2006 *An indoor traction measurement system for agricultural tires*. Journal of Terramechanics.43:317-27.
- [37] **Yahya A, Zohadie, M., Ahmad, D., Elwaleed, A. K., and Kheiralla, A. F.** 2007 *UPM indoor tyre traction testing facility*. Journal of Terramechanics.44:293-301.
- [38] **Woodward AC.** 2011. *Experimental Analysis of the Effects of the Variation of Drawbar Pull Test Parameters for Exploration Vehicles on GRC-1 Lunar Soil Simulant* [Masters]: Virginia Tech.
- [39] **D4643.** *Test Method for Determination of Water (Moisture) Content of Soil by Microwave Oven Heating*. Annual Book of ASTM Standards.4.08.
- [40] **D3282.** *Standard Practice for Classification of Soils and Soil-Aggregate Mixtures for Highway Construction Purposes*. Annual Book of ASTM Standards.04.08.
- [41] **D2487.** *Standard Practice for Classification of Soils for Engineering Purposes (Unified Soil Classification System)*. Annual Book of ASTM Standards.04.08.
- [42] **D698.** *Standard Test Methods for Laboratory Compaction Characteristics of Soil Using Standard Effort (12 400 ft-lbf/ft³ (600 kN-m/m³))*. Annual Book of ASTM Standards.
- [43] **D1883.** *Standard Test Method for CBR (California Bearing Ratio) of Laboratory-Compacted Soils*. Annual Book of ASTM Standards.04.08.
- [44] **D2850.** *Standard Test Method for Unconsolidated-Undrained Triaxial Compression Test on Cohesive Soils*. Annual Book of ASTM Standards.04.08.
- [45] **D2435.** *Standard Test Methods for One-Dimensional Consolidation Properties of Soils Using Incremental Loading*. Annual Book of ASTM Standards.04.08.

9 Appendix

A. Forces acting on wheel due to springs and dampers

The forces acting on the wheel due to the springs and dampers:

$$\begin{aligned} \begin{bmatrix} F_{2,i} \\ F_{7,i} \\ F_{1,i} \end{bmatrix} &= \begin{bmatrix} 0 & 0 & 0 & 0 & 0 & 0 & c_2 & 0 & 0 & c_2 & 0 & 0 & 0 & 0 & 0 \\ 0 & 0 & 0 & 0 & 0 & 0 & 0 & c_7 & 0 & 0 & c_7 & 0 & 0 & 0 & 0 \\ 0 & 0 & 0 & 0 & 0 & 0 & 0 & 0 & c_1 & 0 & 0 & c_1 & 0 & 0 & 0 \end{bmatrix} \dot{q} \\ &+ \begin{bmatrix} 0 & 0 & 0 & 0 & 0 & 0 & k_2 & 0 & 0 & k_2 & 0 & 0 & 0 & 0 & 0 \\ 0 & 0 & 0 & 0 & 0 & 0 & 0 & k_7 & 0 & 0 & k_7 & 0 & 0 & 0 & 0 \\ 0 & 0 & 0 & 0 & 0 & 0 & 0 & 0 & k_1 & 0 & 0 & k_1 & 0 & 0 & 0 \end{bmatrix} q \end{aligned} \quad (9-1)$$

where the first index denotes the direction of the force, and the second one the mass number. Note that the mass number index 0 refers to the rigid wheel.

B. Equations of motion on the Side wall

The forces acting on the springs and dampers connected to the left sidewall are presented in equation (9-2), (9-3) and (9-4).

$$\begin{aligned} \begin{bmatrix} F_{x,i,l} \\ F_{y,i,l} \\ F_{z,i,l} \end{bmatrix} &= \begin{bmatrix} 0 & 0 & 0 & 0 & 0 & 0 & -c_2 - c_6 & 0 & 0 & 0 & 0 & 0 & c_6 & 0 & 0 \\ 0 & 0 & 0 & 0 & 0 & 0 & 0 & -c_7 - c_3 & 0 & 0 & 0 & 0 & 0 & c_3 & 0 \\ 0 & 0 & 0 & 0 & 0 & 0 & 0 & 0 & -c_1 - c_5 & 0 & 0 & 0 & 0 & 0 & c_5 \end{bmatrix} \dot{q} \\ &+ \begin{bmatrix} 0 & 0 & 0 & 0 & 0 & 0 & -k_2 - k_8 & 0 & 0 & 0 & 0 & 0 & k_8 & 0 & 0 \\ 0 & 0 & 0 & 0 & 0 & 0 & 0 & -k_7 - k_5 & 0 & 0 & 0 & 0 & 0 & k_5 & 0 \\ 0 & 0 & 0 & 0 & 0 & 0 & 0 & 0 & -k_1 - k_6 & 0 & 0 & 0 & 0 & 0 & k_6 \end{bmatrix} q \end{aligned} \quad (9-2)$$

$$\begin{aligned} F_{4,i,l} &= k_4(-z_{i-1,l} \sin \Delta\theta + x_{i-1,l} \cos \Delta\theta - x_{i,l}) - k_4(-z_{i+1,l} \sin \Delta\theta - x_{i+1,l} \cos \Delta\theta + x_{i,l}) \\ &+ c_4(-\dot{z}_{i-1,l} \sin \Delta\theta + \dot{x}_{i-1,l} \cos \Delta\theta - \dot{x}_{i,l}) \\ &- c_4(-\dot{z}_{i+1,l} \sin \Delta\theta - \dot{x}_{i+1,l} \cos \Delta\theta + \dot{x}_{i,l}) \end{aligned} \quad (9-3)$$

$$F_{3,i,l} = k_3(x_{i-1,l} \sin \Delta\theta + z_{i-1,l} \cos \Delta\theta - z_{i,l}) - k_3(x_{i+1,l} \sin \Delta\theta - z_{i+1,l} \cos \Delta\theta + z_{i,l}) \quad (9-4)$$

On the other hand, the forces on the right sidewall are the following,

$$\begin{aligned} \begin{bmatrix} F_{x,i,r} \\ F_{y,i,r} \\ F_{z,i,r} \end{bmatrix} &= \begin{bmatrix} 0 & 0 & 0 & 0 & 0 & 0 & 0 & 0 & 0 & -c_2 - c_6 & 0 & 0 & c_6 & 0 & 0 \\ 0 & 0 & 0 & 0 & 0 & 0 & 0 & 0 & 0 & 0 & -c_7 - c_3 & 0 & 0 & c_3 & 0 \\ 0 & 0 & 0 & 0 & 0 & 0 & 0 & 0 & 0 & 0 & 0 & -c_1 - c_5 & 0 & 0 & c_5 \end{bmatrix} \dot{q} \\ &+ \begin{bmatrix} 0 & 0 & 0 & 0 & 0 & 0 & 0 & 0 & 0 & -k_2 - k_8 & 0 & 0 & k_8 & 0 & 0 \\ 0 & 0 & 0 & 0 & 0 & 0 & 0 & 0 & 0 & 0 & -k_7 - k_5 & 0 & 0 & k_5 & 0 \\ 0 & 0 & 0 & 0 & 0 & 0 & 0 & 0 & 0 & 0 & 0 & -k_1 - k_6 & 0 & 0 & k_6 \end{bmatrix} q \end{aligned} \quad (9-5)$$

$$\begin{aligned}
F_{4,i,r} = & k_4(-z_{i-1,r} \sin \Delta\theta + x_{i-1,r} \cos \Delta\theta - x_{i,r}) \\
& - k_4(-z_{i+1,r} \sin \Delta\theta - x_{i+1,r} \cos \Delta\theta + x_{i,r}) \\
& + c_4(-\dot{z}_{i-1,r} \sin \Delta\theta + \dot{x}_{i-1,r} \cos \Delta\theta - \dot{x}_{i,r}) \\
& - c_4(-\dot{z}_{i+1,r} \sin \Delta\theta - \dot{x}_{i+1,r} \cos \Delta\theta + \dot{x}_{i,r})
\end{aligned} \tag{9-6}$$

$$F_{3,i,r} = k_3(x_{i-1,r} \sin \Delta\theta + z_{i-1,r} \cos \Delta\theta - z_{i,r}) - k_3(x_{i+1,r} \sin \Delta\theta - z_{i+1,r} \cos \Delta\theta + z_{i,r}) \tag{9-7}$$

C. Equation of motion Belt and Tread

The forces acting on the belt and tread elements due to the connected springs and dampers are described below,

$$\begin{aligned}
& \begin{bmatrix} F_{x,i,bt} \\ F_{y,i,bt} \\ F_{z,i,bt} \end{bmatrix} \\
& = \begin{bmatrix} 0 & 0 & 0 & 0 & 0 & 0 & c_6 & 0 & 0 & c_6 & 0 & 0 & -2c_6 & 0 & 0 \\ 0 & 0 & 0 & 0 & 0 & 0 & 0 & c_3 & 0 & 0 & c_5 & 0 & 0 & -2c_3 & 0 \\ 0 & 0 & 0 & 0 & 0 & 0 & 0 & 0 & c_5 & 0 & 0 & c_5 & 0 & 0 & -2c_5 \end{bmatrix} \dot{q} \\
& + \begin{bmatrix} 0 & 0 & 0 & 0 & 0 & 0 & k_8 & 0 & 0 & k_8 & 0 & 0 & -2k_8 & 0 & 0 \\ 0 & 0 & 0 & 0 & 0 & 0 & 0 & k_5 & 0 & 0 & k_5 & 0 & 0 & -2k_5 & 0 \\ 0 & 0 & 0 & 0 & 0 & 0 & 0 & 0 & k_6 & 0 & 0 & k_6 & 0 & 0 & -2k_6 \end{bmatrix} q
\end{aligned} \tag{9-8}$$

As such, the equations of motion for the belt and tread layer are defined by equation

$$M_{i,bt} \ddot{q}_{i,bt} = \begin{bmatrix} F_{x,i,bt} \\ F_{y,i,bt} \\ F_{z,i,bt} \end{bmatrix} + \begin{bmatrix} -m_{i,bt}g \cos(\theta_i + \nu) + F_{xcp,i,bt} \\ -F_{ycp,i,bt} \\ -m_{i,bt}g \sin(\theta_i + \nu) - m_{i,bt}R_{i,bt}\dot{\nu}^2 + \sigma_{n,i,bt} \end{bmatrix} \tag{9-9}$$

D. Shear Stress

$$\left(1 - e^{-\frac{R_i[(\theta_a - \theta_e) - (\cos \theta_e - \cos \theta_a) + s_d(\cos \theta_e - \cos \theta_a)]}{k_x}}\right)^2 + \left(1 - e^{-\frac{R_i(1-s_d)(\theta_a - \theta_e) \tan \alpha_c}{k_y}}\right)^2 = 1 \tag{9-10}$$

$$F_{xcp,i} = \begin{cases} \tau_{x,i} S_i W_i & \theta_e \geq \theta \geq \theta_a \\ \frac{\mu_x^2 s_d}{\sqrt{(\mu_y \tan \alpha_c)^2 + (\mu_x s_d)^2}} \tau_{max,i} S_i W_i & \theta_a > \theta \geq \theta_r \end{cases} \tag{9-11}$$

$$F_{ycp,i} = \begin{cases} \tau_{y,i} S_i W_i & \theta_e \geq \theta \geq \theta_a \\ \frac{\mu_y^2 \tan \alpha_c}{\sqrt{(\mu_y \tan \alpha_c)^2 + (\mu_x s_d)^2}} \tau_{max,i} S_i W_i & \theta_a > \theta \geq \theta_r \end{cases} \tag{9-12}$$

where μ_x and μ_y are the friction coefficients; and they are computed using Eq. (48).